

Kineo: Calibration-Free Metric Motion Capture From Sparse RGB Cameras

CHARLES JAVERLIAT, École Centrale de Lyon, CNRS, INSA Lyon, Université Claude Bernard Lyon 1, Université Lumière Lyon 2, LIRIS, UMR5205, ENISE, France

PIERRE RAIMBAUD, École Centrale de Lyon, CNRS, INSA Lyon, Université Claude Bernard Lyon 1, Université Lumière Lyon 2, LIRIS, UMR5205, ENISE, France

GUILLAUME LAVOUÉ, École Centrale de Lyon, CNRS, INSA Lyon, Université Claude Bernard Lyon 1, Université Lumière Lyon 2, LIRIS, UMR5205, ENISE, France

Markerless multiview motion capture is often constrained by the need for precise camera calibration, limiting accessibility for non-experts and in-the-wild captures. Existing calibration-free approaches mitigate this requirement but suffer from high computational cost and reduced reconstruction accuracy. We present Kineo, a fully automatic, calibration-free pipeline for markerless motion capture from videos captured by unsynchronized, uncalibrated, consumer-grade RGB cameras. Kineo leverages 2D keypoints from off-the-shelf detectors to simultaneously calibrate cameras, including Brown-Conrady distortion coefficients, and reconstruct 3D keypoints and dense scene point maps at metric scale. A confidence-driven spatio-temporal keypoint sampling strategy, combined with graph-based global optimization, ensures robust calibration at a fixed computational cost independent of sequence length. We further introduce a pairwise reprojection consensus score to quantify 3D reconstruction reliability for downstream tasks. Evaluations on EgoHumans and Human3.6M demonstrate substantial improvements over prior calibration-free methods. Compared to previous state-of-the-art approaches, Kineo reduces camera translation error by approximately 83-85%, camera angular error by 86-92%, and world mean-per-joint error (WMPJPE) by 83-91%. Kineo is also efficient in real-world scenarios, processing multi-view sequences faster than their duration in specific configuration (e.g., 36min to process 1h20min of footage). The full pipeline and evaluation code are openly released to promote reproducibility and practical adoption at: liris-xr.github.io/kineo.

CCS Concepts: • **Computing methodologies** → **Reconstruction**.

Additional Key Words and Phrases: human pose estimation, motion capture, markerless, calibration-free

1 Introduction

Motion capture technology is an essential tool for converting physical movement into digital representations. Traditional optical systems (e.g., OptiTrack [30], Vicon [51], Qualisys [36]) rely on multiple calibrated infrared cameras that track reflective markers placed on key locations of the subject’s body. An animated skeletal model is then reconstructed for the motion to be analyzed or re-targeted on a virtual character for a realistic animation. While these systems achieve sub-millimeter accuracy in controlled studio conditions, they require subjects to wear optical markers, which can induce behavioral biases and make their use challenging or impractical. Moreover, deployment for in-the-wild scenarios (e.g., outdoor sport,

theatrical performances or concerts, craftsmanship), or for casual users (e.g., home fitness, motion-based gaming) presents significant challenges: the setup requires careful calibration, controlled lighting with limited infrared perturbations, and precise marker placement on the body. All cameras are wired together for temporal synchronization and connected to power outlets, limiting their use for on-location recordings in uncontrolled environments. Furthermore, the specialized hardware and controlled studio conditions significantly restrict the accessibility of these systems due to their high cost.

Recent advancements in computer vision and deep learning have led to the development of markerless motion capture methods. These approaches enhance accessibility by eliminating the need for optical markers and utilizing consumer-grade RGB cameras. Despite these advancements, some challenges persist: monocular methods are subject to depth ambiguities and occlusions, and multi-view methods necessitate precise camera calibration and synchronization. Many existing methods assume the availability of pre-calibrated, synchronized, cameras, which can be a limiting factor, especially in non-studio settings. In such uncontrolled environments, cameras are often placed to accommodate different scenes or subjects. Calibration is typically performed using a known pattern like a checkerboard or a wand, and temporal synchronization by using dedicated hardware or software during capture. Although effective, the calibration process can be tedious and error-prone, especially for non-experts. Improper calibration can make the footage unusable, as incorrect camera calibration and synchronization prevent the use of methods that assume known camera parameters.

Calibration-free methods have been explored to address these challenges by recovering camera parameters post-capture using video and audio information, eliminating the need for calibration procedures. While great progress has been made recently, especially in reconstructing the cameras, humans, and scene in metric scale [29, 38], calibration-free approaches remain relatively underexplored, and there is still significant potential for improvement in terms of accuracy, scalability to long sequences by reducing computational cost, and practicality for downstream tasks. In particular, current methods suffer from pipeline inefficiencies such as heavy reliance on multiple computationally intensive neural network models, the use of parametric model representations and iterative nonlinear optimization on individual frames. These factors collectively limit the scalability to long video sequences on commodity hardware. Moreover, many approaches lack 3D confidence measures, which are

Authors’ Contact Information: Charles Javerliat, charles.javerliat@ec-lyon.fr, École Centrale de Lyon, CNRS, INSA Lyon, Université Claude Bernard Lyon 1, Université Lumière Lyon 2, LIRIS, UMR5205, ENISE, Saint-Etienne, France; Pierre Raimbaud, pierre.raimbaud@ec-lyon.fr, École Centrale de Lyon, CNRS, INSA Lyon, Université Claude Bernard Lyon 1, Université Lumière Lyon 2, LIRIS, UMR5205, ENISE, Saint-Etienne, France; Guillaume Lavoué, guillaume.lavoue@enise.ec-lyon.fr, École Centrale de Lyon, CNRS, INSA Lyon, Université Claude Bernard Lyon 1, Université Lumière Lyon 2, LIRIS, UMR5205, ENISE, Saint-Etienne, France.

essential for accurately quantifying uncertainty in the reconstructed geometry.

In this context, we introduce Kineo, a fully automatic, calibration-free pipeline for markerless motion capture from videos captured by unsynchronized, uncalibrated, consumer-grade RGB cameras. Our method fully leverages 2D keypoints from off-the-shelf detectors to simultaneously automatically calibrate cameras (including Brown–Conrady distortion coefficients) and reconstruct 3D keypoints and dense scene point maps at metric scale. A novel confidence-driven keypoint sampling strategy, combined with graph-based optimization, ensures a fixed computational cost for the automatic calibration step, independent of the sequence duration. Additionally, we introduce the pairwise reprojection confidence score, which quantifies the reliability of 3D estimations for downstream tasks. Unlike previous calibration-free methods, our optimization process does not rely on parametric body models or complex neural network architectures; instead, Kineo follows the traditional Structure-from-Motion (SfM) paradigm, while fully leveraging the high precision and accurate confidence scores of recent 2D keypoint detectors. This simple freeform formulation enables our method to consider the entire sequence in the optimization, by selecting the most reliable keypoint correspondences across frames and views, leading to improvements in both accuracy and computational efficiency. Additionally, Kineo’s keypoint-based approach is inherently modular: improved 2D detectors can be integrated seamlessly without altering the architecture, instantly enhancing calibration and reconstruction accuracy. In summary, our main contributions are:

- **Confidence-Aware Spatio-Temporal Subsampling.** We introduce a novel keypoint correspondence spatio-temporal sampling strategy that uses 2D detector confidences to select high-quality matches for robust and more efficient RANSAC based Structure-from-Motion for essential-matrix estimation.
- **Graph-Based Global Calibration.** We model the camera network as a weighted graph, assign edge weights a pairwise calibration quality metric (average Sampson distance), and extract a minimum spanning tree (MST) to initialize an optimal global configuration of camera extrinsics.
- **3D Confidence.** We lift 2D confidences into 3D by defining a *pairwise reprojection confidence score* for each triangulated point that can be used for downstream tasks.
- **Model-Agnostic and SMPL-Based Scale Recovery.** To address global scale ambiguity, we evaluate two independent approaches: (1) a model-agnostic method using monocular metric depth estimation, and (2) a human-prior-based method that leverages the SMPL model when people are present in the scene.
- **Distortion-Aware Calibration.** Unlike prior works, we explicitly estimate and incorporate Brown–Conrady distortion coefficients into our pipeline, enabling accurate camera calibration and robust 3D reconstruction even with consumer-grade RGB cameras prone to lens distortion.

We evaluate our approach on the EgoHumans and Human3.6M datasets, demonstrating substantial improvements over prior calibration-free methods. Compared to previous state-of-the-art approaches,

Kineo reduces camera translation error by approximately 83–85%, camera angular error by 86–92%, and world mean-per-joint error (WMPJPE) by 83–91%. We validate Kineo’s applicability in real-world settings, both in offline and online, real-time scenarios. Notably, Kineo’s computational efficiency allows for processing extended sequences faster than their actual duration. For example, processing six views of five-minute videos at 50Hz, totaling a cumulated footage duration of 30 minutes, requires only 11 minutes of processing on an NVIDIA RTX 3080 Ti, highlighting its practicality for real-world deployment on commodity hardware. To encourage further research and practical adoption, we release our pipeline and evaluation code as open source at liris-xr.github.io/kineo.

2 Related Work

Achieving markerless motion capture in uncontrolled environments, particularly for non-expert users, requires addressing several challenges to enable a fully automated pipeline. These challenges include synchronizing battery-powered cameras, estimating camera parameters without manual calibration, resolving global metric scale, and maintaining computational efficiency suitable for consumer-grade hardware. Although recent advances in computer vision and deep learning have significantly enhanced the accessibility of markerless motion capture, especially in monocular settings, many multiview methods still rely on pre-calibrated, synchronized camera setups or assume known intrinsics and extrinsics. These constraints limit their practicality in real-world or casual scenarios where such prerequisites are unavailable without manual calibration. In contrast, our work targets the calibration-free setting, aiming to operate directly on raw, unsynchronized video streams without requiring specialized hardware or manual setup.

In the following, we review related work across five key dimensions central to our method: (1) temporal synchronization, (2) automatic camera calibration, (3) metric scale recovery, (4) 3D confidence estimation, and (5) performance and system-level considerations. We cover both classical geometric pipelines and recent learning-based approaches, emphasizing the assumptions they make, their applicability in uncontrolled environments, and their relevance to the broader goal of general-purpose calibration-free motion capture.

2.1 Temporal Synchronization

Temporal synchronization refers to the process of recovering the time offset between the camera internal clock and a global time reference to express the timestamps of each frame in a shared world time reference. Temporal synchronization is essential in multi-view motion capture to synchronize camera frames, as even small temporal offsets between cameras can lead to inaccuracies in the reconstruction due to visual differences in the observed poses across views, especially when dealing with fast movements [5, 44, 52]. Traditional studio camera systems rely on physical wiring to trigger all cameras simultaneously. However, such hardware-based synchronization is not available or impractical when using consumer-grade devices like smartphones or action cameras. Alternatively, jam syncing can be used. This technique synchronizes the internal clocks of multiple recording devices by transferring a timecode from a master device to slave devices. The synchronization must be performed at the

start of the recording and periodically throughout the session to prevent clock drift. Once the slave devices receive the timecode, they operate independently while remaining aligned with the master device’s time reference. Importantly, jam syncing requires dedicated hardware [46] or software [24] at capture time. When dedicated synchronization hardware or software is unavailable or was not used during capture, post-capture temporal synchronization methods can be employed. Among these, audio-based techniques have been used [11, 43]. These methods leverage the sound captured by each camera to find the time offsets (temporal extrinsics). Hasler et al. [11] use cross-correlation on the audio signal using Fast Fourier Transform; the audio delay between the signals is found by locating the peak of the cross-correlation. When cameras are located at varying distances from the sound source, differences in audio propagation time can cause desynchronization. For instance, a 20-meter distance difference between two cameras recording at 60 Hz would lead to an estimated misalignment of around 4 frames. However, such large disparities are rare in practice, since the sound is typically emitted by the subject, who is usually positioned near the center of a circular or spherical camera setup. In these configurations, the propagation delay is negligible. Even in this worst-case scenario, the resulting 4-frame misalignment can still serve as a coarse initial estimate for image-based synchronization methods. These methods use visual information, typically human pose, from the different cameras to refine the time offset but assume that an initial coarse temporal alignment is provided for the optimization. Shuai et al. [44] include the time offset as a variable to be optimized within a joint estimation framework, assuming identical frame rates between all cameras. Vo et al. [52] optimize frame rate, rolling shutter pixel readout speed and time offset. To perform sub-frame alignment, those methods interpolate poses to a common time frame for their optimization process. Shuai et al. [44] estimate joint velocities using finite differences, allowing them to interpolate poses using a first-order approximation. While computationally efficient, this approach is sensitive to noise. To improve robustness, Akhter et al. [1] proposed using Discrete Cosine Transform (DCT) for interpolating the values, which is less sensitive to noise. This strategy was subsequently adopted in later works [15, 52]. More recently, Choi et al. [6] proposed using dynamic time warping (DTW) between every pair of videos to compute a constant time offset that minimizes the distance between 3D joint positions, extracted from estimated SMPL models obtained via SLAHMR [61] for each video individually. Their method achieves subframe accuracy without requiring coarse alignment. However, it involves constructing an $N \times N$ matrix containing all possible pose associations to find the optimal time offset that minimizes the 3D joint distances, which can become a computational bottleneck for large sequences.

Ultimately, while image-based synchronization offers improvements in temporal precision, the practical balance of accuracy, speed, and ease of use tends to favor audio-based methods for most consumer-grade multi-view capture scenarios, where sound propagation delay is negligible. To further explore this trade-off, our method builds upon Hasler et al.’s audio synchronization approach. We employ a more compact audio feature representation for efficient cross-correlation. Additionally, we derive mathematical expressions

that define camera distance thresholds for fixed audio analysis parameters or, conversely, the required audio analysis parameters for given camera distances, below which sub-frame synchronization accuracy using audio alone is achievable, as detailed in Section 4.

2.2 Automatic Camera Calibration

Accurate estimation of camera parameters, both intrinsics (e.g., focal length, principal point, distortion coefficients) and extrinsics (position and orientation), is essential for multi-view 3D reconstruction. Examples include the use of such parameters in methods that first regress 2D keypoints or features and subsequently lift them into 3D space through techniques such as triangulation [5, 56, 62] or volumetric fusion [17, 35, 49, 60]. In optimization-based pipelines, the estimated camera parameters are used to reproject 3D structures (commonly a SMPL model or skeletal representation) into 2D space, minimizing the reprojection error with respect to the observed 2D cues. While these methods exploit accurate camera parameters, most assume access to ground-truth values provided by datasets or obtained through manual calibration, rather than estimating them. This section focuses on existing methods for automatically estimating camera intrinsics and extrinsics.

2.2.1 Camera Intrinsics. Camera intrinsics refer to the internal characteristics of the camera, typically represented in the intrinsic matrix K . These include the focal length, principal point (the intersection of the optical axis with the image plane), and skew (often negligible). In the idealized pinhole camera model, these parameters are sufficient for projection. However, real-world lenses introduce optical distortions that cause straight lines in the scene to appear curved in the image.

High-fidelity intrinsic calibration is essential in both monocular and multi-view systems, as it directly impacts the accuracy of the 2D–3D mapping through the projection operation. In monocular regression-based approaches that predict 3D structure directly from 2D inputs, having access to precise intrinsics at inference time has shown to improve the quality of the reconstruction [3, 8, 20, 32, 39]. Incorporating intrinsics into the network inputs enables more generalizable performance compared to methods using a simplified model of orthographic projection or fixed training-set intrinsics. These simplified models introduce a camera bias, resulting in a trade-off: achieving more accurate 3D pose estimates can come at the expense of poorer alignment with 2D image features, and vice versa [8, 20].

In multi-view reconstruction, intrinsics are equally critical. Both in methods where intrinsics are used to unproject the 2D keypoints or features into a shared 3D space [17, 35, 49, 60] or in optimization-based methods when computing the reprojection loss to align the 3D model with 2D cues [13, 29].

Because camera intrinsics are fixed properties of the camera itself and independent of its viewpoint, they can be obtained through offline calibration after data capture. Consequently, some methods relax the constraints on obtaining these parameters by using ground truth intrinsics, assuming the camera is accessible for later calibration and thus only focus on recovering the camera extrinsics [6, 13, 56]. However, this assumption limits applicability in

scenarios involving online videos, unknown camera setups, or fully calibration-free approaches.

Several learning-based methods have been proposed to enable calibration-free inference by estimating camera parameters directly from image data. Within the Human Pose Estimation domain, some monocular approaches focus on estimating the camera field of view from images containing humans [20, 32] to feed them to the body shape and pose regression model or for later optimization.

More recently, multiview approaches have also incorporated intrinsic parameter estimation. For instance, HAMSt3R [38] builds upon DUST3R [55] and MAST3R [25], recovering intrinsics from the predicted depth maps but with a model specialized for human-centric reconstruction which yields better reconstruction quality. Similarly, Müller et al. [29] leverage MAST3R to initialize camera intrinsics that are subsequently refined in a global optimization loop. Both methods remain tailored to human subjects and do not estimate distortions coefficients. More broadly, other learning-based methods have been introduced for general-purpose applications, predicting both the focal length and lens distortion parameters [4, 47, 50], or just the camera focal length [25, 54, 54, 55] from RGB images. In our method, we adopt the general model MoGe [54] to predict an initial camera focal length for each view (see Sec. 5.1). The focal length is subsequently optimized in the bundle adjustment step (see Sec. 5.6). To our knowledge, Human Pose Estimation methods, whether monocular or multiview, typically assume distortion-free inputs, relying on ground-truth calibration to undistort images as a preprocessing step prior to reconstruction or evaluation or simply neglecting distortion altogether. In contrast, our pipeline also estimates distortion coefficients, following the Brown–Conrady model, by integrating them in the bundle adjustment (see Sec. 5.6), enabling accurate handling of lens distortion and improving multi-view consistency.

2.2.2 Camera Extrinsics. Camera extrinsics define the position and orientation of a camera within a shared world coordinate system. They are represented as a rigid transformation consisting of a rotation matrix R and a translation vector \mathbf{t} , which map 3D points from world to camera coordinates. Accurate extrinsics are critical for multi-view motion capture, as they enable consistent integration of information across cameras. Misestimated extrinsics lead to geometric misalignment, resulting in inaccurate 3D reconstructions.

Various approaches have been proposed to estimate extrinsics in multi-camera setups, broadly falling into learning-based human-centric methods and classical geometric Structure-from-Motion (SfM) approaches.

Learning-based human-centric methods often leverage strong priors on human shape and pose. Choi et al. [6] first estimate monocular human motion in each view using SLAHMR [61], which predicts SMPL body meshes per frame. They compute an initial extrinsic estimate by minimizing per-joint distances to align motions across views, followed by refinement using a NeRF-based photometric optimization. This achieves sub-degree rotational and sub-centimeter translational errors on the CMU Panoptic Studio dataset.

Hewitt et al. [14] adopt a PnP-based strategy, aligning 3D head meshes with 2D facial landmarks, following the method introduced by Szymanowicz et al. [45]. The head serves as a stable reference

as its overall shape remains relatively stable across facial expressions and head poses. Initial estimates are refined through direct optimization of camera rotations and translations.

Müller et al. [29] use DUST3R [55] to predict dense 3D pointmaps from image pairs, recover relative poses, and integrate them into a global optimization that simultaneously updates SMPL models, scene pointmaps, and camera parameters. Similarly, HAMSt3R [38], trained specifically on human-centric scenes, aligns multiple views using predicted pairwise pointmaps within a common global frame, based on the method from DUST3R [55].

Despite differences, these methods share a reliance on parametric body models (e.g., SMPL or SOMA) or human-specific scene training. Such priors provide strong constraints that help resolve global scale ambiguities, as body shape enforces a consistent metric scale, but are computationally intensive, especially when optimization to refine initial camera poses and body poses is involved, like in HSfM [29].

Classical SfM approaches estimate extrinsics by exploiting geometric correspondences between views. Frameworks like COLMAP [40] perform incremental bundle adjustment using traditional feature matching. While computationally efficient, these methods are sensitive to noise, outliers, and unreliable correspondences.

Outlier rejection is commonly implemented by embedding the estimation algorithm within a RANSAC framework [34, 56], which robustly estimates relative camera poses from noisy keypoint correspondences. However, uniform random sampling in long sequences is often inefficient: matches from unreliable regions may be repeatedly sampled, while spatially clustered keypoints contribute redundant geometric information. To address this, we introduce a confidence-weighted spatio-temporal subsampling strategy that prioritizes high-confidence, spatially diverse keypoints, ensuring robustness and fixed computational cost.

Early motion-capture SfM approaches also exploited semantic cues from the human body, including silhouette extrema [22, 28, 48], bounding box centers [57], and 2D keypoints [34, 56], with keypoints proving particularly robust for establishing correspondences.

UnCaliPose [56] follows a similar principle, using 2D keypoints to estimate initial camera poses that are later refined through joint bundle adjustment with 3D human poses. Although effective, the method depends on ground-truth intrinsics and distortion coefficients, does not reconstruct the scene, and shows limited accuracy in metric-scale outputs. To improve calibration, UnCaliPose adopts a two-step approach, first calibrating cameras across multiple frames and then solving for human poses, but the paper does not specify how these frames are selected. Without a selection strategy, incorporating all frames makes joint bundle adjustment computationally infeasible for long sequences. Our approach builds upon this framework by also leveraging 2D keypoints, but extends it to estimate camera intrinsics and distortion parameters, reconstruct a scene pointmap (as in HSfM and HAMSt3R), and produce metric-scale results with confidence estimates. Our spatio-temporal keypoint sampling ensures both high quality automatic calibration and scalable computational cost during bundle adjustment.

Once pairwise relative poses are estimated using SfM, the next step is to recover the global camera calibration by composing these

pairwise transformations into a consistent network. Greedy strategies, such as selecting the next camera based on maximum inliers [34] or minimal average alignment angle [56], offer efficiency, but accumulate errors and provide a suboptimal solution. In addition, relative extrinsics computed via SfM are only determined up to an unknown scale factor, which must be resolved to properly compose them into the absolute extrinsics. Xu et al. [56] address this by leveraging the fixed length of bones in 3D space to resolve scale ambiguities between camera pairs. However, this approach requires that the bone is visible and well triangulated by all camera pairs involved, which may not always be the case in challenging capture scenarios.

We reformulate calibration as a graph problem: cameras are nodes, pairwise calibrations forming the edges are weighted by a pairwise calibration score, and a minimum spanning tree yields the globally optimal calibration. This formulation, that can be found in literature as the essential graph, allows us to solve for the relative scales via loop closure constraints, and to find the optimal camera network configuration via the use of a minimum spanning tree. To recover the global scale, we explore two approaches. The first leverages a monocular metric geometry estimator, MoGe [54] that we use to predict per-view depth maps in real-world units. This allows the reconstruction to be rescaled accurately and removes the need for any category-specific parametric model. The second approach draws inspiration from prior work using human body models; we estimate global scale as a downstream step using the shape priors of the SMPL model. Both strategies preserve the efficiency of a classical Structure-from-Motion pipeline while enabling metric-scale reconstruction. As a result, our method produces calibrated cameras, 3D keypoints, and a point cloud of the surrounding scene, matching the outputs of previous works.

2.3 3D Confidence

Although the literature in 3D reconstruction focuses on recovering structure from monocular or multi-view input, most methods do not provide an explicit confidence score that correlates with reconstruction quality. Yet, such confidence estimates are critical for downstream tasks such as hypothesis fusion, temporal smoothing, and filtering, where occlusions and uncertain predictions must be handled appropriately.

Deterministic methods, which produce a single 3D estimate from one or more images, typically do not model uncertainty. Their output is unique, making it difficult to assess or compare reliability across views or time. This limitation is particularly problematic in multi-view scenarios, where certain views may be significantly more informative than others due to occlusion or pose ambiguity. In the absence of confidence scores, all views are treated equally during fusion, which can lead to suboptimal results.

To overcome this, probabilistic approaches have been introduced to model uncertainty by predicting distributions over plausible 3D poses. For example, ProHMR [21] and HumaniFlow [42] sample multiple hypotheses from learned distributions, allowing per-joint or per-vertex uncertainty to be estimated from the variance of the samples. These uncertainty estimates enable view-consistent fusion—either by optimizing the joint probability across views or by

weighting individual predictions in a fusion step according to their confidence. However, this expressiveness comes at the cost of computational efficiency, as accurate uncertainty estimation typically requires drawing a large number of samples.

More efficient alternatives such as POCO [7] have been proposed to address this trade-off. POCO extends deterministic models by directly predicting uncertainty alongside the 3D output, eliminating the need for sampling. While significantly faster, such methods remain tightly coupled to parametric models and are not readily applicable to non-parametric 3D representations such as lifted keypoints.

In this work, we introduce a simple and effective confidence metric tailored to lifted 3D keypoints in multi-view settings, independent of any body model. Our approach defines 3D confidence as the weighted mean reprojection agreement across all views, where each view contribution is modulated by its 2D keypoint confidence. This formulation reflects how well the 3D reconstruction aligns with available 2D evidence, prioritizing views with reliable observations. The resulting score captures both geometric consistency and detection confidence, while remaining lightweight and applicable to a broad range of scenarios. We provide a detailed description in Section 6.

2.4 Output Representation and Performance Considerations

Despite substantial progress in markerless motion capture, many recent methods remain computationally intensive, rendering them impractical for long video sequences or deployment on consumer-grade hardware. For example, on an NVIDIA V100 GPU, HSfM requires over 100 seconds to process a single 4-view frame with three subjects, while HAMSt3r takes 14 seconds. To put this into perspective, processing a 20-minute video at 25 frames per second would require approximately 40 days for HSfM and 4 days for HAMSt3r.

This limitation stems from the use of computationally heavy models applied to each frame individually and, in the case of HSfM, from an additional optimization loop involving numerous parameters, which further increases computational complexity.

A major source of complexity in this optimization arises from the type of 3D representation used. Parametric models [12, 27, 33] are widely adopted due to their compactness and strong structural priors. These models encode pose and shape in low-dimensional spaces, enabling them to represent plausible pose and shape configurations even under occlusions or depth ambiguities. Such priors are particularly valuable in single-view settings, where geometric constraints are crucial to resolve ambiguity. However, in multiview scenarios, where ambiguities are naturally reduced through additional viewpoints, these structural constraints become less critical. The computational cost of parametric models remains high due to the multiple transformation stages required (e.g., pose decoding from latent space[33], blendshape evaluation, linear blend skinning), as well as the iterative fitting needed to align model projections with 2D image evidence for each video frame. Moreover, these models are typically constrained to specific subject categories, such as humans, and are subject to biases like mean-shape bias [39, 41].

By contrast, non-parametric models, including keypoints, voxels, point clouds, etc., offer a more direct and computationally efficient alternative but do not provide inherent constraints. Keypoint-based representations, in particular, are widely used in multiview and optimization-based pipelines due to their lightweight nature. While they lack explicit structural constraints, soft priors can be introduced to guide the optimization toward plausible solutions [5]. In cases where such priors are omitted, we refer to the models as *free-form* non-parametric representations. A hybrid strategy has also emerged, wherein non-parametric predictions are converted to parametric models parameters for compactness and use in downstream tasks. In particular, Sáráandi et al. [39] propose a fast method to fit SMPL meshes to dense non-parametric 3D keypoints.

Hybrid pipelines that combine learning-based regressors with subsequent optimization have shown strong performance and enhanced robustness in challenging scenarios. A representative example is HSfM, a calibration-free method that achieves good accuracy by leveraging multiple specialized models to jointly reconstruct cameras, scenes and human subjects. Specifically, HSfM employs SAM2[37] for segmentation, HMR2.0[9] for pose regression, DUST3R[55] to estimate the scene and cameras, ViTPose[58] for keypoint detection, and SMPL[27] for body modeling. These components provide complementary information that, when refined through a global optimization stage, lead to SOTA quality reconstructions. However, this architecture also increases computational complexity and results in longer runtimes due to the integration of several heavyweight models.

Our method achieves superior performance both in speed and accuracy through a more frugal architecture, leveraging only a monocular geometry estimator and a 2D keypoint detector. This minimal yet effective combination reduces inference time significantly, while improving reconstruction accuracy. Our approach enables faster and more scalable processing, making it suitable for long video sequences and consumer-grade hardware.

Beyond algorithmic complexity, existing pipelines are limited by system-level inefficiencies. Most existing methods operate on frames that are pre-extracted from video streams, introducing preprocessing delays and significant disk usage, especially for high-resolution or long-duration videos. To eliminate this overhead, we incorporate hardware-accelerated GPU decoding directly into our pipeline, avoiding the need to store or read individual frames. Furthermore, we extend MMPose to support fully GPU-resident, batched keypoint inference, removing redundant CPU-GPU transfers. These system-level improvements enable real-time performance with minimal memory and disk overhead. The resulting architecture is modular, facilitating the integration of alternative keypoint detectors and strategies with minimal effort.

3 Method overview

We propose a pipeline for performing markerless motion capture from uncalibrated and unsynchronized cameras. The pipeline is designed to handle both human and non-human subjects, including scenes with multiple individuals. It outputs metric-space 3D

keypoints, scene point maps, and complete camera parameters, including extrinsics, intrinsics, and Brown–Conrady distortion coefficients. The pipeline is designed for modularity and efficiency, enabling scalable processing of long video sequences. An overview of the pipeline is shown in Figure 1.

Given videos from unsynchronized and uncalibrated cameras, the pipeline first estimates temporal offsets between video streams via audio-based synchronization, aligning keypoint detections on a shared global timeline (see Sec. 4).

Next, automatic camera calibration is performed using 2D keypoints detected by a replaceable off-the-shelf detector. A graph-based formulation is used to recover an optimal global camera configuration through minimum spanning tree selection. Central to the robustness and efficiency of this stage is our keypoint sampling strategy proposed in Sec. 5.2.1, which selects high-confidence correspondences to reduce noise and outliers while ensuring computational efficiency. This stage also estimates lens distortion parameters, which are often neglected by other approaches (see Sec. 5).

Using the estimated cameras, scene pointmaps and skeletons are reconstructed in arbitrary units. We assign a novel confidence score to the triangulated keypoints, the pairwise reprojection confidence score (see Sec. 6.3), which we leverage during the metric-scale recovery stage to enhance robustness and reliability (see Sec. 7).

To obtain metric-scale reconstructions, we propose two strategies. The first leverages a human body prior, using the SMPL model when people are present in the scene, similar in concept to HSfM [29]. The second is subject-agnostic, employing a monocular metric depth estimator to recover scale even in scenes without humans (see Sec. 7).

4 Temporal Synchronization

To relate 2D cues from different viewpoints, we must estimate temporal offsets between the videos. This is particularly important for battery-powered, unsynchronized cameras, where hardware-based synchronization is unavailable or impractical for easy-to-deploy setups. We adopt an audio-based approach that computes the temporal lag γ_k for each camera by aligning its audio track with that of a reference camera using cross-correlation. To know when sub-frame synchronization accuracy can be achieved using audio alone, we provide mathematical expressions that specify either the camera distance thresholds for fixed audio analysis parameters or the required audio analysis parameters for known camera distances.

Rather than relying on raw spectrogram cross-correlation, which is computationally demanding for long recordings [11, 43], we use compact audio descriptors to improve efficiency. Specifically, we represent each audio track using Mel-Frequency Cepstral Coefficients (MFCCs), a perceptually motivated and widely adopted feature in audio analysis. MFCCs capture the spectral envelope of the signal and are robust to noise. The reduced set of features allows for efficient and accurate cross-correlation, making them a suitable choice for estimating temporal lag in multi-camera settings.

The accuracy of this method depends on two main factors: the temporal resolution of the MFCC representation and the physical distance between the sound source and each camera. The former is determined by the hop length H used during the Short-Time

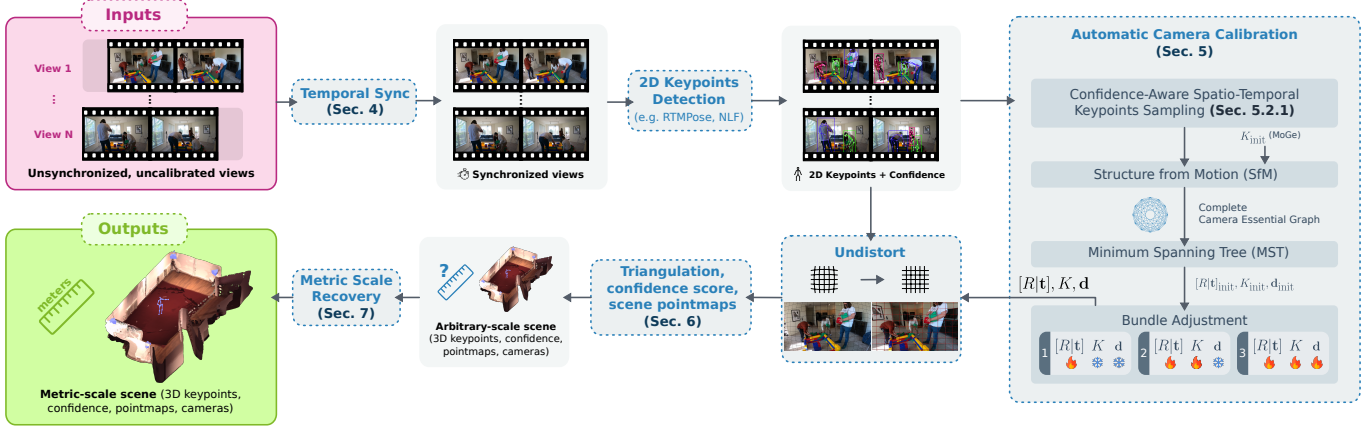


Fig. 1. Overview of the Kineo pipeline for markerless motion capture from uncalibrated and unsynchronized multi-camera videos. Starting from raw video inputs, the system first performs audio-based temporal synchronization to align unsynchronized streams on a shared timeline. Next, automatic camera calibration estimates extrinsic and intrinsic parameters, including Brown–Conrady lens distortion, via a graph-based optimization over 2D keypoint correspondences selected by a confidence-driven sampling strategy. Using the recovered cameras, 3D keypoints and scene point maps are reconstructed, and each triangulated keypoint is assigned a pairwise reprojection confidence score to quantify reconstruction quality. Finally, metric-scale recovery is achieved either through a human body prior using the SMPL model or a monocular metric depth estimator for subject-agnostic scaling. The modular design enables robust and scalable reconstruction of both human and non-human subjects across long, multi-view sequences.

Fourier Transform (STFT), and the latter by the time delay resulting from different distances to the sound source. Following prior observations [11], we formalize these two sources of error as Δt_1 and Δt_2 , respectively. We derive conditions under which subframe synchronization is achievable. Let f_s be the audio sample rate, f_r the video frame rate, H the hop length, d_1 and d_2 the distance from each camera to the sound source respectively, and $c \approx 343$ m/s the speed of sound in air. Then:

$$\Delta t_1 = \frac{H}{2f_s} \quad \text{and} \quad \Delta t_2 = \frac{|d_1 - d_2|}{c}$$

Subframe accuracy is ensured when the combined error is below a video frame duration:

$$\Delta t_1 + \Delta t_2 < \frac{1}{f_r}$$

Which yields the following constraints:

$$H < \frac{2f_s}{f_r} - \frac{2f_s|d_1 - d_2|}{c} \quad \text{and} \quad |d_1 - d_2| < c\left(\frac{1}{f_r} - \frac{H}{2f_s}\right)$$

These inequalities guide the choice of hop length H given the approximate scene geometry, or conversely, define the spatial constraints required for accurate synchronization when H is fixed.

In typical multi-view camera arrangements (e.g., circular rigs), microphone distances to the sound source vary by only a few meters. For instance, with $|d_1 - d_2| < 5$ m, $f_s = 48$ kHz, and $f_r = 60$ Hz, the hop length H must be below 200 samples to ensure subframe accuracy. Inversely, with $H = 1$, the method remains accurate for inter-microphone distances below approximately 5.7 m. In case finer alignment is required, image-based synchronization techniques [44, 52] can be used to refine an initial audio-based estimate. In all experiments presented in this work, the camera setups fall within our constraints, and audio-based synchronization is sufficient to

achieve subframe accuracy. As a result, we did not incorporate image-based refinement in our pipeline.

5 Graph-based Automatic Camera Calibration

Recovering accurate camera extrinsics and intrinsics is essential for leveraging multi-view setups: without proper calibration, 3D reconstruction suffers from misalignments and degraded accuracy in downstream tasks. At the same time, manual calibration is impractical, especially for in-the-wild deployments.

We address the problem of automatic and efficient calibration of camera networks by modeling the multi-view system as a graph. Each node corresponds to a camera C_i , and edges represent pairwise relative geometry between two cameras C_i and C_j , encoded by the essential matrix E_{ij} . These essential matrices are estimated via robust RANSAC-based Structure-from-Motion (SfM) on a subsampled high-confidence keypoint correspondences set (see Section 5.2.1). Edge weights reflect calibration quality, quantified by the average Sampson distance over inliers.

This graph formulation enables global reasoning about pairwise relationships and allows us to select an optimal subset of calibrations through a minimum spanning tree (MST). This contrasts with prior incremental approaches that add cameras greedily to a global frame, at the risk of yielding a suboptimal global configuration [34, 56]. By composing relative poses along the MST, we recover global camera extrinsics efficiently with a guarantee of minimizing the total calibration error (Section 5.5). The recovered cameras are expressed in arbitrary units, and metric scaling to real-world dimensions is applied in Sec. 7.

5.1 Intrinsic Initialization

To construct the camera graph, we need to recover the relative poses between camera pairs, which requires decomposing the essential matrices into their corresponding rotations and translation directions. Computing the essential matrix, however, depends on knowledge of the camera intrinsics K . In our scenario, where cameras are assumed to be static and the subject is moving, Kruppa’s formulation [10, 23] cannot be applied. One alternative is to compute fundamental matrices, which do not require intrinsics, and then optimize the intrinsics for each camera by minimizing the Sampson distance over all edges. However, full-graph optimization is computationally expensive, growing exponentially with the number of cameras. To maintain a linear cost with respect to the number of cameras, we instead use MoGe [54] to obtain an initial estimate of each camera’s intrinsics. This model is later reused to predict scene point maps. These intrinsics are later refined during bundle adjustment (Sec. 5.6), to which we incorporate lens distortion coefficients that follow the Brown-Conrady model, a step omitted in prior works.

5.2 Efficient Pairwise Calibration

We propose a novel approach for pairwise camera calibration that is both robust and scalable to long sequences due to its fixed computational cost. Our method builds upon the work of Puwein et al. [34] by introducing confidence-driven spatio-temporal subsampling of keypoint correspondences, which enhances robustness while maintaining efficiency. Additionally, we leverage a graph-based formulation to compute relative scales reliably, incorporating the quality of each pairwise calibration to produce geometrically consistent relative extrinsics.

The edges of the graph represent pairwise camera calibrations, encoded by an essential matrix E_{ij} that captures the relative rotation R_{ij} and translation direction \hat{t}_{ij} between cameras C_i and C_j . Classical approaches estimate this matrix using the Structure-from-Motion (SfM) five-point algorithm [31] within a RANSAC loop applied either to all raw keypoint correspondences [56] or to a subset of correspondences [34]. Both strategies can be unstable when low-quality correspondences are present, and processing all correspondences becomes computationally prohibitive for long sequences.

Learning-based methods such as DUST3r [29, 55] predict relative poses in a single-frame multiview setting and can be more robust when high-confidence keypoints are unavailable. However, they do not exploit temporal consistency, which can limit accuracy, and their reliance on an additional neural network increases computational overhead; for example, DUST3r requires approximately 40 ms for inference on a single image pair using an H100 GPU. In contrast, our method is more computationally frugal because it fully exploits the same 2D keypoints that are already required for triangulating the final skeleton output. By selectively subsampling these keypoints based on their detection confidence, we improve the stability and accuracy of previous approaches while preserving the efficiency of classical SfM and ensuring scalability to long sequences.

5.2.1 Confidence-Aware Spatio-Temporal Subsampling. An effective spatio-temporal subsampling strategy for keypoint correspondences is important for three reasons: (1) it improves the robustness

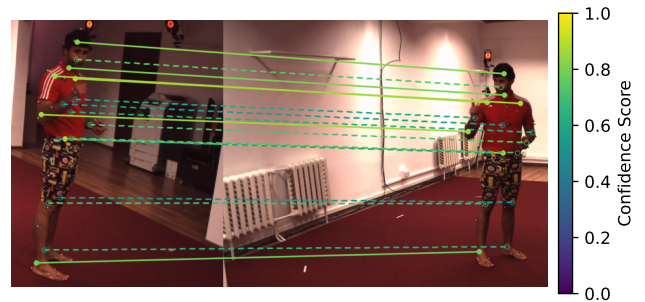


Fig. 2. Example confidence-driven keypoint subsampling for a pair of views from Human3.6M. Colors indicate the pair confidence score $w_{k,l}$, solid lines represent selected correspondences, and dashed lines represent correspondences that were not selected. The sampling favors keypoints for which the 2D keypoint detector is highly confident about their location (e.g., unoccluded and well-localized keypoints).

of essential matrix estimation by filtering out low-quality correspondences and by leveraging information across multiple frames, (2) it reduces computational complexity by limiting the number of correspondences, which is particularly important for scalability on long sequences, and (3) it preserves sufficient geometric diversity to ensure accurate essential matrix estimation. Traditional RANSAC samples correspondences uniformly, ignoring the varying reliability of detections. As a result, if low-confidence correspondences constitute a majority, they can disproportionately influence hypothesis generation, leading to inaccurate relative pose estimates and requiring more iterations to converge on a valid model. Puwein et al. [34] addressed this by sampling correspondences with higher probabilities for temporally distant correspondences and for those involving different keypoints. However, their strategy does not leverage keypoint confidence scores, which can lead to the inclusion of unreliable correspondences.

Building on their method, we improve the spatio-temporal subsampling strategy by incorporating the 2D keypoints detector confidence scores $w_{i,k} \in [0, 1]$, with i the view index and k the keypoints index, into the selection process. Each point correspondence between camera C_i and C_j is denoted as $(\mathbf{x}_{i,k}, \mathbf{x}_{j,k})$. Its score is computed as the geometric mean of the detector confidences:

$$w_{ij,k} = \sqrt{w_{i,k} \cdot w_{j,k}} \quad (1)$$

Only correspondences with $w_{ij,k} > \tau$ are retained. From this filtered pool, a final set of M correspondences is randomly selected to implicitly promote temporal diversity and geometric coverage. An example of this confidence-driven subsampling is shown in Fig. 2. This final set of correspondences is then used in the standard RANSAC loop to generate hypotheses and remove any remaining outliers while estimating the essential matrices.

5.3 Graph Edge Reliability Estimation

To assess the reliability of pairwise camera calibration, we measure the geometric consistency between its corresponding points set. To make this measure independent of camera intrinsics, the points are first normalized by their intrinsic calibration matrix estimated in

Sec. 5.1:

$$\hat{\mathbf{x}}_{i,k} = K_i^{-1} \mathbf{x}_{i,k} \text{ and } \hat{\mathbf{x}}_{j,k} = K_j^{-1} \mathbf{x}_{j,k}$$

The normalized Sampson distance for correspondence k is:

$$\mathcal{S}(E_{ij}, \hat{\mathbf{x}}_{i,k}, \hat{\mathbf{x}}_{j,k}) = \frac{(\hat{\mathbf{x}}_{j,k}^\top E_{ij} \hat{\mathbf{x}}_{i,k})^2}{(E_{ij} \hat{\mathbf{x}}_{i,k})_x^2 + (E_{ij} \hat{\mathbf{x}}_{i,k})_y^2 + (E_{ij}^\top \hat{\mathbf{x}}_{j,k})_x^2 + (E_{ij}^\top \hat{\mathbf{x}}_{j,k})_y^2}$$

Finally, the calibration score for the camera pair is computed as the average Sampson distance, evaluated over all RANSAC inlier correspondences:

$$s_{ij} = \frac{1}{M} \sum_{m=1}^M \mathcal{S}(E_{ij}, \hat{\mathbf{x}}_{i,m}, \hat{\mathbf{x}}_{j,m}) \quad (2)$$

This score is used as the weight of the edge connecting cameras C_i and C_j in the calibration graph, reflecting the reliability of their relative pose.

5.4 Solving relative scales

The essential matrix E_{ij} is only defined up to a relative scale factor λ_{ij} . Formally, given its decomposition into a relative rotation $R_{ij} \in SO(3)$ and a translation direction $\hat{\mathbf{t}}_{ij} \in \mathbb{R}^3$, the relation between two camera poses is expressed as:

$$R_j = R_i R_{ij} \text{ and } \mathbf{t}_j = R_i \cdot (\lambda_{ij} \cdot \hat{\mathbf{t}}_{ij}) + \mathbf{t}_i$$

In previous work, finding this relative scale λ_{ij} is addressed by aligning 3D structures in a common space. Xu et al. [56] rescale and align the triangulated bones from each camera pair into a shared coordinate system. In their method, the quality of the pairwise triangulation directly affects the result when computing the relative scales. Methods like DUS3r [55] incorporate the scaling factors into a global alignment loop. The predicted pairwise point maps are then scaled and aligned into a globally consistent 3D reconstruction.

Instead, we solve for the relative scales λ_{ij} by exploiting loop closure constraints [2]. The key idea is that if we follow the relative transformations along a closed cycle of cameras, for example moving from C_i to C_j to C_k and back to C_i , we should return to the starting point. This concept is illustrated in Fig. 3. Formally, each triplet of cameras yields one linear constraint of the form:

$$\lambda_{ij} R_{ki} R_{jk} \hat{\mathbf{t}}_{ij} + \lambda_{jk} R_{ki} \hat{\mathbf{t}}_{jk} + \lambda_{ki} \hat{\mathbf{t}}_{ki} = \mathbf{0} \quad (3)$$

We collect all L loop constraints into a homogeneous linear system $A\boldsymbol{\lambda} = \mathbf{0}$, where $A \in \mathbb{R}^{3L \times M}$ contains the coefficients from the constraints, and $\boldsymbol{\lambda} \in \mathbb{R}^M$ represents the unknown relative scale factors.

Not all loop closure constraints are equally reliable. Some camera pairs (edges in the graph) may have less accurate essential matrices. Consequently, loops that include these less reliable edges are also less trustworthy. To account for this, we leverage the edge weights computed in Sec. 5.3 to weight the loop closure constraints. Specifically, we define a loop score as the geometric mean of the scores of its three edges:

$$s_{ijk} = \sqrt[3]{s_{ij} s_{jk} s_{ki}} \quad (4)$$

By arranging these scores into a diagonal matrix $W \in \mathbb{R}^{L \times L}$, we formulate the weighted homogeneous system:

$$W A \boldsymbol{\lambda} = \mathbf{0} \quad (5)$$

We solve this system using a nonlinear least-squares. This formulation admits the trivial solution $\boldsymbol{\lambda} = \mathbf{0}$, and otherwise the solution is only determined up to a global scale factor. A common way to remove this ambiguity is to fix one variable, e.g. set $\lambda_{01} = 1$. However, this can bias the solution in systems with many loop constraints where λ_{01} is underrepresented. In such cases, all $\boldsymbol{\lambda}$ values tend to shrink toward zero to minimize the loss, except for the fixed $\lambda_{01} = 1$. When composing the relative extrinsics into absolute extrinsics (see Sec. 5.5), this often leads to inconsistent solutions, such as two clusters of cameras separated by the long translation scaled by λ_{01} . To avoid this, we instead add a regularization term that encourages all $\boldsymbol{\lambda}$ values to stay close to 1. Formally, we solve the following optimization problem:

$$\min_{\boldsymbol{\lambda}} \|W^{\frac{1}{2}} A \boldsymbol{\lambda}\|_2^2 + \mu \|\boldsymbol{\lambda} - \mathbf{1}\|_2^2 \quad (6)$$

where μ is the regularizer weight. In practice, we use the L-BFGS algorithm and solve for the logarithm of $\boldsymbol{\lambda}$ to ensure the exponentiated values remain positive.

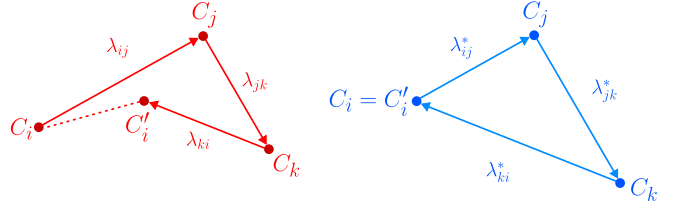


Fig. 3. Example of camera loop closure with incorrect (left) and correct (right) relative scale factors. When the relative scales λ_{ij} are incorrect, traversing the cycle $C_i \rightarrow C_j \rightarrow C_k \rightarrow C'_i$ does not return to the original camera position, resulting in $C_i \neq C'_i$. In contrast, when the correct scales are used, the composition of the relative transformations yields the identity, and the loop closes consistently with $C_i = C'_i$.

5.5 Optimal Absolute Extrinsic

Having estimated relative extrinsics, the next step is to recover the absolute poses of all cameras in a common global frame. Naively chaining relative transformations along arbitrary paths in the camera graph can lead to error accumulation, especially when some edges are less reliable. To ensure optimality, we use the calibration reliability scores computed in Sec. 5.3 to guide edge selection.

We define the first camera C_0 as the origin with pose $[R | \mathbf{t}]_0 = [I | \mathbf{0}]$, where I is the identity rotation matrix and $\mathbf{0}$ the zero translation vector. Since multiple paths may connect C_0 to a camera C_k , each path accumulates errors differently depending on the quality of the relative transforms. To minimize total error, we construct a minimum spanning tree (MST) of the camera graph using Kruskal's algorithm, with edge weights corresponding to pairwise calibration reliability computed in Sec. 5.3. Absolute extrinsics are then computed by composing relative transformations along the unique MST path from C_0 to each camera C_k . Formally, if P_k^* denotes this optimal path, the absolute pose $[R | \mathbf{t}]_k$ is obtained as

$$[R | \mathbf{t}]_k^* = \prod_{(i,j) \in P_k^*} [R | \mathbf{t}]_{ij} = \prod_{(i,j) \in P_k^*} \begin{bmatrix} R_{ij} & \lambda_{ij} \hat{\mathbf{t}}_{ij} \\ \mathbf{0}^T & 1 \end{bmatrix}, \quad (7)$$

where R_{ij} and $\hat{\mathbf{t}}_{ij}$ are the relative rotation and unit translation vector from camera C_i to C_j , and λ_{ij} is the relative scale factor computed in Sec. 5.4. This MST-based initialization provides a robust starting point for the subsequent bundle adjustment, which further refines camera poses and reduces residual errors.

5.6 Bundle Adjustment

The MST-based initialization described in Sec. 5.5 provides a solid starting point for absolute camera extrinsics. However, residual errors remain due to the linear estimation being used in estimating pairwise essential matrix estimation. Similarly, the intrinsics initialized in Sec. 5.1 are only approximate and assume a simplified pinhole model without accounting for lens distortions. While other methods overlook distortions parameters, often undistorting images using the ground-truth parameters, we propose to integrate the distortion coefficients as a parameter to be optimized in the bundle adjustment.

Optimizing over all detected keypoints across the sequence is computationally prohibitive. Instead, we refine camera parameters using a carefully selected subset of points, deferring triangulation of the full sequence to a later stage. Following the strategy in Sec. 5.2.1, we subsample keypoints to maintain fixed computational cost and ensure scalability for long sequences. We select keypoints that are confidently detected in at least two views, which is the minimum requirement for triangulation:

$$\sum_{i=1}^N \mathbf{1}[w_{i,k} > \kappa] \geq 2, \quad (8)$$

where N is the number of views, κ is a minimum keypoint confidence threshold and $\mathbf{1}[\cdot]$ the indicator function (equals 1 if the condition holds, 0 otherwise). The selected keypoints are then uniformly subsampled to a maximum of M keypoints, and are triangulated to initialize the optimization, denoted as $\mathbf{X}_m \in \mathbb{R}^3$.

Bundle adjustment proceeds in three passes, with optimized parameters gradually added at each stage. In the first pass, only camera poses (extrinsics) and 3D points are optimized to reduce misalignments, while intrinsic parameters remain fixed. In the second pass, we jointly optimize camera poses, 3D points and focal lengths. In the final and third pass, distortion coefficients are added, following the Brown-Conrady model, which accounts for both radial and tangential distortions. In every pass, the optimization goal is to minimize the weighted average reprojection error of the 3D points across all views:

$$\epsilon_{i,m} = \|\pi(K_i, \mathbf{d}_i, [R|\mathbf{t}]_i, \mathbf{X}_m) - \mathbf{x}_m\|_2 \quad (9)$$

The residuals are then aggregated into a robust, weighted loss function using a Huber loss $H_\delta(\cdot)$, where each residual is weighted by the 2D detector confidence $w_{i,m} \in [0, 1]$ for the corresponding keypoint:

$$\mathcal{L}_{\text{reproj}} = \frac{\sum_{i=1}^N \sum_{m=1}^M w_{i,m} H_\delta(\epsilon_{i,m})}{\sum_{i=1}^N \sum_{m=1}^M w_{i,m}} \quad (10)$$

Here, N is the number of views, M the number of 3D points, $\epsilon_{i,m}$ is the normalized reprojection residuals, $\pi(\cdot)$ denotes the projection function, K_i is the intrinsic matrix, \mathbf{d}_i the Brown-Conrady distortion coefficients, and $[R | \mathbf{t}]_i$ the camera extrinsics. This formulation ensures that the optimization focuses on geometric misalignment

while being robust to outliers and comparable across cameras with different resolutions or focal lengths.

Upon completion of bundle adjustment, the method yields refined camera extrinsics and intrinsics, as well as estimated lens distortion coefficients, which are typically not obtained by alternative approaches. The resulting camera extrinsics, however, are expressed in an arbitrary scale, and global scale still needs to be estimated to convert the reconstructed scene into metric units.

6 3D Output And Confidence Score

Given accurate camera extrinsics and intrinsics, lifting 2D keypoints to 3D and reconstructing scene pointmaps can be formulated as downstream tasks. In this section, we describe the methods used for scene pointmap estimation and for triangulating and estimating the confidence for 3D keypoints.

6.1 Scene Pointmaps

We evaluated two models to reconstruct the scene pointmaps: MoGe [54] and VGGT [53]. For both methods, each input image is first undistorted using the predicted distortion coefficients.

MoGe, being a monocular method, predicts a dense pointmap in camera space for each view, which is then merged into a global pointmap in world space using the camera extrinsics. To further improve prediction quality, we undistort the image using the estimated distortion coefficients, and provide MoGe with the camera focal length estimated in earlier stages (see Sec. 5.1 and Sec. 5.6).

In contrast, VGGT takes multiple views as input to jointly predict global pointmaps and camera poses. Since VGGT outputs its own camera parameters, we compute a similarity transform to align VGGT’s predicted cameras with ours and apply this transform to the scene pointmap. Although this alignment is approximate due to VGGT’s cameras being less accurate than ours, this approach yields pointmaps that are more spatially consistent across views than those obtained with MoGe. However, VGGT is considerably more computationally intensive, and its complexity increases with the number of input cameras.



(a) Scene pointmap generated with MoGe. (b) Scene pointmap generated with VGGT.

Fig. 4. Comparison of scene pointmaps produced by two geometry estimation models. (a) shows the pointmap generated with MoGe, which uses single-view images and camera intrinsics to produce metric pointmaps. (b) shows the pointmap generated with VGGT, which leverages multiple views to predict a globally consistent pointmap and camera poses, aligned to our camera system. VGGT provides more spatially consistent pointmaps across views, while MoGe relies on single-view depth estimation.

6.2 Triangulation and Confidence Score

The 2D keypoints are lifted to 3D space through a triangulation process using a weighted Direct Linear Transform (DLT) method. This process begins by first undistorting the 2D keypoints using the estimated distortion parameters. Subsequently, the undistorted keypoints are triangulated to determine their 3D positions, leveraging information from all N views. Crucially, the triangulation is weighted by the 2D confidence score of each individual keypoint, $w_{i,m}$. This weighting allows the reconstruction to account for varying levels of uncertainty across different views, thereby improving the accuracy and robustness of the final 3D keypoint coordinates. As the pipeline takes any 2D keypoints as input, the system can generate multiple output formats to suit diverse downstream applications. Figure 5 illustrates this flexibility, showing examples of 3D reconstructions in COCO-19, COCO-133, Human3.6M keypoint formats, as well as a full parametric SMPL body model. The SMPL reconstruction is obtained by first detecting NLF [39] surface keypoints and subsequently fitting them using the *SMPLFitter* module from NLF.

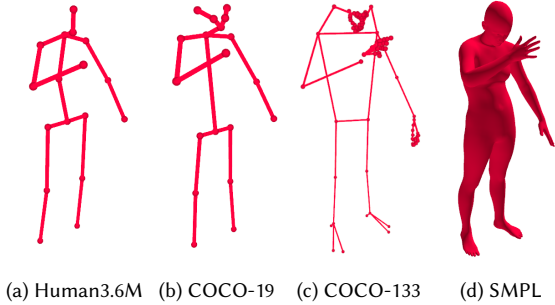


Fig. 5. Examples of different output formats with different 2D keypoints detectors used by Kineo. (a–c) show keypoint-based representations in various formats, while (d) illustrates a full parametric SMPL body reconstruction. For the SMPL model, NLF surface keypoints are first detected and subsequently fitted using the *SMPLFitter* module from NLF.

6.3 Pairwise Reprojection Confidence Score

Associating a confidence score to the lifted 3D keypoints is crucial for downstream tasks that leverage the reliability of information from reconstructed points (e.g. filtering, weighted metrics). When reconstructing a 3D point from multiple camera views, not all points are equally reliable. Some may be consistent across views, while others may vary due to noise or occlusions. We propose a confidence score that captures how well a 3D point aligns with the 2D detections across all cameras. Simply put, if most views agree on where the point should be, the 3D point is more trustworthy.

For a 3D point \mathbf{X}_m , we first measure how well it projects back into each camera i compared to the observed 2D detection \mathbf{x}_m . We normalize the reprojection residual by the camera’s focal length to remove the effect of varying pixel scales, allowing errors to be compared across cameras with different intrinsics:

$$\tilde{\epsilon}_{i,m} = \frac{\|\pi(K_i, \mathbf{d}_i, [R|t]_i, \mathbf{X}_m) - \mathbf{x}_m\|_2}{f_i} \quad (11)$$

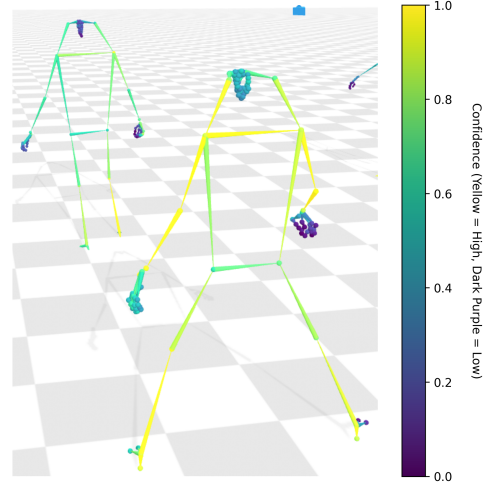


Fig. 6. Visualization of the proposed *pairwise reprojection consensus score* on 3D human skeleton reconstructions from the *EgoHumans* dataset, obtained using Kineo. The low score in poorly reconstructed hands demonstrates how the proposed confidence correlates with reconstruction quality and could be leveraged for downstream filtering; note that we did not implement this filtering in our method and leave it for future work.

To transform the residual into a score within the range $[0, 1]$, where higher scores indicate lower residuals, we apply an exponential decay function:

$$s_{i,m} = \exp(-\lambda \tilde{\epsilon}_{i,m}) \quad (12)$$

We measure agreement between each pair of views using the geometric mean of their scores, weighted by the 2D detection confidences. This ensures that pairs with more reliable 2D points contribute more to the score, reflecting the importance of accurate reprojection for confident detections:

$$s_{ij,m} = \sqrt{w_i \cdot w_j} \sqrt{s_{i,m} \cdot s_{j,m}} \quad (13)$$

Finally, we compute the overall 3D point confidence s_m by averaging the scores of all view pairs:

$$s_m = \frac{N(N-1)}{2} \sum_{i=1}^{N-1} \sum_{j=i+1}^N s_{ij,m} \quad (14)$$

This gives a final confidence between 0 and 1: points with high consistency across multiple confident views get a high score, while noisy or unreliable points get a low score. Because the score is based on pairs of views, at least one valid pair is required for the score to be greater than 0. This naturally ensures that the 3D point is triangulated from at least two views, which is a necessary condition for the reconstruction to be meaningful. Qualitative examples of how these confidence scores reflect the quality of reconstructed keypoints are shown in Figure 6.

7 Metric Scale Recovery

The absolute extrinsics we estimated are defined only up to a global scale, which limits their applicability in downstream tasks requiring metric scale. Unlike methods relying solely on parametric body

models to resolve scale ambiguity, which depend on the presence of humans in the scene, we propose two different strategies for global scale recovery: one specific for scenes involving humans and one that is generic and broadly applicable, enabling metric-scale reconstruction even for non-human subjects.

7.1 SMPL-based Scale Estimation

The first approach estimates the global scale factor by leveraging the SMPL parametric body model. Conceptually, this approach is related to the method of Müller et al. [29], which incorporates the SMPL model within a global optimization loop to constrain the solution space to metric-consistent configurations. However, our method differs in how the SMPL body prior is used to extract the global scale. Specifically, we treat scale estimation as a downstream task rather than integrating it into a global optimization. This avoids potential conflicts between camera and body shape objectives, reducing the risk of being stucked in local minima. Given a skeleton in arbitrary units, we formulate an optimization problem to recover the correct global scale. The goal is to determine the scale factor α that maps the arbitrary-unit skeleton to metric space while enforcing the same body proportions between the two skeletons by updating the SMPL shape parameters β . This optimization is computationally efficient, as it only requires estimating body shape, ignoring pose, and thus eliminating the need for linear blend skinning. This approach is illustrated in Fig. 7.

Formally, the unposed SMPL model is defined by the function $V = M(\beta)$, where $\beta \in \mathbb{R}^{10}$ represents the shape parameters and $V \in \mathbb{R}^{6890 \times 3}$ denotes the body vertices. Skeleton keypoints are obtained from the SMPL model using a regressor $J^{K \times 6890}$, yielding $\hat{\mathbf{j}} \in \mathbb{R}^{K \times 3}$:

$$\hat{\mathbf{j}}(\beta) = M(\beta) \cdot J \quad (15)$$

Let $\mathbf{j} \in \mathbb{R}^{K \times 3}$ be the 3D skeleton keypoints in arbitrary units, and let S denote the set of bones defined by skeleton connectivity. For a given global scale α , these keypoints are mapped to the SMPL model space as $\alpha\mathbf{j}$. Hence, bone lengths in this common space are computed as:

$$\ell_{kl} = \alpha \|\mathbf{j}_k - \mathbf{j}_l\|_2 \quad \text{and} \quad \hat{\ell}_{kl} = \|\hat{\mathbf{j}}_k - \hat{\mathbf{j}}_l\|_2 \quad (k, l) \in S \quad (16)$$

Leveraging the 3D confidence of the keypoints estimated in Sec. 6.3, we define the confidence of each bone as the geometric mean of the confidences of its two endpoint keypoints. This formulation ensures that if either joint is estimated with low confidence, the corresponding bone length is considered unreliable:

$$s_{kl} = \sqrt{s_k \cdot s_l} \quad (17)$$

To ensure stable convergence, we initialize the SMPL shape parameters β to the mean shape, i.e., the null vector, and set the initial scale factor α_0 as the weighted average ratio between the bone length of the skeleton in arbitrary units and the SMPL skeleton bones:

$$\beta_0 = \mathbf{0} \quad \text{and} \quad \alpha_0 = \frac{\sum_{(k,l) \in S} s_{kl} \frac{\hat{\ell}_{kl}}{\ell_{kl}}}{\sum_{(k,l) \in S} s_{kl}} \quad (18)$$

We optimize α and β using the L-BFGS optimizer by minimizing a loss that enforces both bone length consistency and plausible body

shape:

$$\mathcal{L}_{\text{bones}} = \frac{\sum_{(k,l) \in S} s_{kl} \mathcal{H}_\delta(\ell - \hat{\ell})}{\sum_{(k,l) \in S} s_{kl}} \quad \text{and} \quad \mathcal{L}_\beta = \|\beta\|_2^2 \quad (19)$$

Where \mathcal{H}_δ is the Huber loss for robustness to outliers (e.g. bones with excessive length due to occlusion). The total loss is expressed as:

$$\mathcal{L}_{\text{tot}} = \lambda_{\text{bones}} \mathcal{L}_{\text{bones}} + \lambda_\beta \mathcal{L}_\beta \quad (20)$$

The final optimized α^* is used to rescale the skeletons, scene pointmaps, and cameras.

7.2 Metric Depth-based Scale Estimation

While the previous SMPL-based approach is effective at recovering global scale, it is limited to footage including humans due to its reliance on a parametric body model. We overcome this restriction by using a monocular metric depth estimator, MoGe [54], which can estimate a metric depth map from a monocular RGB image. Since MoGe can take the focal length as input to improve output quality, we feed it the intrinsics estimated in previous stages (see Sec. 5.1 and Sec. 5.6). The global scale α is computed as the ratio between the joint depths in metric units obtained from the depth map and the corresponding joint depths in arbitrary units. This approach is illustrated in Fig. 8.

Formally, given the camera extrinsics $[R \mid \mathbf{t}]$, and the skeleton keypoints $\mathbf{j} \in \mathbb{R}^{K \times 3}$, the keypoints depth corresponds to the z coordinate of the joint in camera space:

$$\mathbf{j}_{\text{cam}} = \begin{bmatrix} x_c \\ y_c \\ z_c \end{bmatrix} = [R \mid \mathbf{t}] \cdot \mathbf{j}, \quad d_a = z_c \quad (21)$$

Let $D \in \mathbb{R}^{H \times W \times 1}$ be the predicted depthmap, we sample the metric depth using the projected keypoints coordinates, using both the intrinsics K and distortion coefficients \mathbf{d} :

$$\mathbf{j}_{\text{img}} = \begin{bmatrix} u \\ v \end{bmatrix} = \pi(K, \mathbf{d}, [R|\mathbf{t}]; \mathbf{j}), \quad d_m = D_{v,u} \quad (22)$$

The global scale factor is computed as the ratio between the distance in metric units and the distance in arbitrary units $\alpha = d_m/d_a$. In practice, we select a single frame for each view, choosing the one with the most reliable keypoints. Reliability is quantified by a heuristic score that evaluates how well the 3D keypoints reproject onto the given view:

$$h_i = \frac{1}{K} \sum_{k=1}^K \exp(-\lambda \epsilon_{i,k}) \quad (23)$$

where K denotes the number of keypoints and $\epsilon_{i,k}$ represents the reprojection residuals as defined in Eq. 9. The exponential decay function transforms the residuals into a score within the interval $[0, 1]$, such that higher values correspond to lower reprojection errors. The frame with the maximum score h_i is selected for each view.

Next, we sample depth values at the keypoint locations in the selected frames, considering only those keypoints whose confidence $w_{i,k}$ exceeds a threshold ζ . This filtering avoids erroneous depth comparisons in regions where a joint is unlikely to be present. Finally, the global scale factor is estimated as the weighted average of

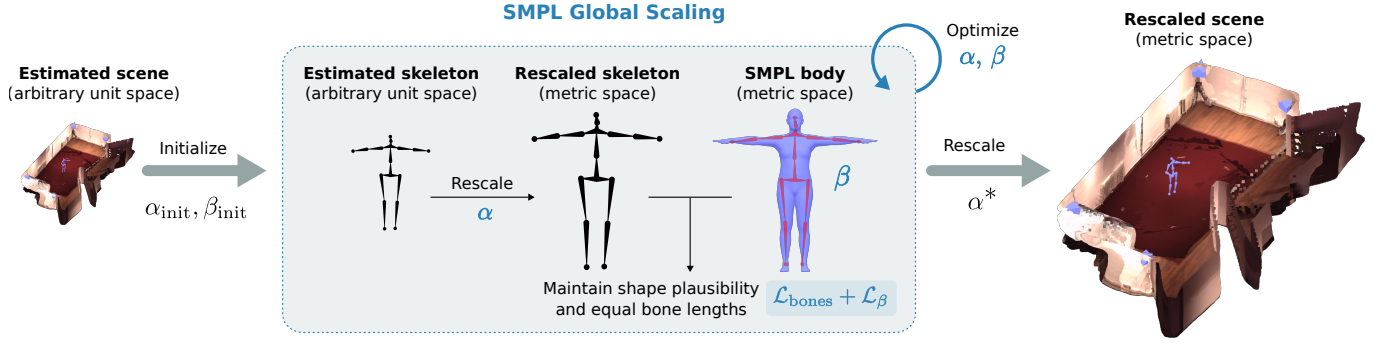


Fig. 7. Overview of SMPL-based global scaling. The SMPL body model serves as a prior for metric scale, providing plausible human body proportions that guide the estimation of the global scale factor α , which converts the scene from arbitrary units to metric units. Given an estimated skeleton in arbitrary units, we optimize α while updating the SMPL shape parameters β so that the SMPL skeleton closely matches the proportions of the input skeleton, enforced by $\mathcal{L}_{\text{bones}}$ while remaining in the space of plausible, metric-consistent shapes, enforced by \mathcal{L}_{β} . The resulting optimized scale α^* is then applied to rescale the entire scene, including the skeletons, cameras, and scene pointmaps, producing a metric-scale representation.

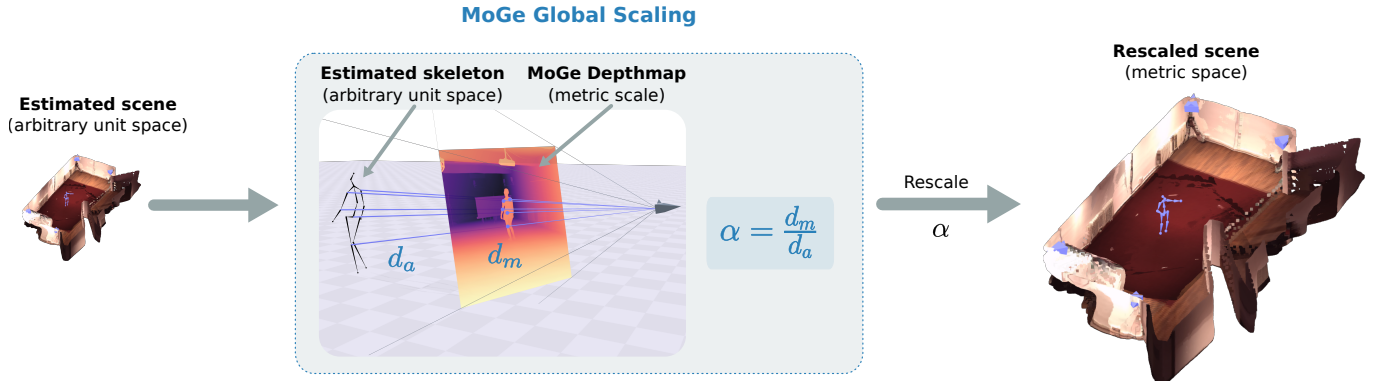


Fig. 8. Overview of metric depth-based global scaling. Unlike SMPL-based scaling, which relies on a parametric human body model, metric depth-based scaling is subject-agnostic, as the metric depth map predicted directly from a the RGB image by MoGe [54] is independent of the subjects present in the scene. The global scale factor α is computed as the ratio between the joint depths in metric units obtained from the depth map and the corresponding joint depths in arbitrary units. The resulting scale α is then applied to rescale the entire scene, including the skeletons, cameras, and scene pointmaps, producing a metric-scale representation.

the ratios between metric distances and distances in arbitrary units across all views:

$$\alpha = \frac{\sum_{i=1}^N \sum_{k=1}^K w_{i,k} \frac{d_{m,k}}{d_{a,k}}}{\sum_{i=1}^N \sum_{k=1}^K w_{i,k}}. \quad (24)$$

The factor α is used to rescale the skeletons, scene pointmaps, and cameras.

8 Experiments

We conduct a comprehensive evaluation of our method through both comparative and ablation studies to assess automatic camera calibration accuracy, 3D reconstruction quality and scalability to long sequences. We begin by establishing the experimental framework, including datasets and evaluation metrics. We then present quantitative comparisons against state-of-the-art methods, followed

by systematic ablation studies to evaluate the contributions to performance of each component in our pipeline. Throughout our evaluation, we demonstrate that our approach achieves substantial improvements over existing calibration-free reconstruction methods while maintaining scalability for practical deployments.

8.1 Experimental Setup

Datasets. We evaluate our method on two complementary datasets that together provide comprehensive coverage of both controlled and in-the-wild scenarios. Human3.6M [16] provides highly accurate ground-truth annotations from a Vicon motion capture system, making it well-suited for evaluating joint localization accuracy and inference speed in controlled, single-person scenarios. Ego-Humans [19] presents more complex scenarios with both indoor and outdoor settings, multiple interacting subjects, frequent occlusions, and dynamic motions, enabling a thorough assessment of our method’s robustness under realistic, unconstrained conditions.

Notably, EgoHumans recordings are captured with GoPro cameras that exhibit significant lens distortion, making this dataset particularly valuable for evaluating the quality of our distortion coefficient estimation, a capability that distinguishes our method from prior approaches that typically ignore distortions or undistort the images with the ground-truth distortions coefficients.

Evaluation Metrics. We assess both joint position accuracy and camera parameters quality using a comprehensive set of standard metrics. Following Müller et al. [29], the predicted scene is first aligned with the ground truth based on camera centers prior to evaluation. For 3D joints reconstruction, we report the World Mean Per Joint Position Error (W-MPJPE), which quantifies the average Euclidean distance between predicted and ground-truth joint positions in the metric world coordinate system. To isolate local pose errors from global misalignment and scale variations, we also report the Procrustes-Aligned MPJPE (PA-MPJPE), computed per subject and per frame after applying a similarity transform from the predicted skeleton to the ground truth. For camera pose, we report the Translation Error (TE), in meters, and Angular Error (AE), in degrees, to quantify deviations in position and orientation from the ground truth. Complementing these error metrics, we report the Camera Center Accuracy (CCA) [26], which measures the proportion of estimated camera centers within predefined distance thresholds relative to the scene scale, and the Relative Rotation Accuracy (RRA), defined as the percentage of cameras whose angular error falls below specified thresholds. To decouple positional errors from global scale, we additionally compute scale-aligned variants by applying a similarity transformation that aligns and uniformly scales the estimated scene to the ground truth, resulting in the scale-aligned Translation Error (s-TE) and scale-aligned Camera Center Accuracy (s-CCA). Finally, we report the Field-of-View error (FoV), in degrees, to quantify deviations between the estimated and ground-truth camera field of view.

Implementation Details. Throughout all experiments, we assume known cross-view re-identification of subjects, focusing our evaluation on the core calibration and reconstruction components. For 2D keypoint detection, we primarily employ NLF as our detector due to its balance of accuracy and efficiency, though we also evaluate alternative detectors in our ablation studies. Unless otherwise specified, we use our SMPL-based global scale estimation and report results without post-processing or filtering applied to the reconstructed joints. All experiments are conducted on a workstation equipped with an Nvidia Tesla A100 GPU and an AMD Milan EPYC 7543 CPU.

8.2 Quantitative Evaluation

We benchmark our method against state-of-the-art multi-view reconstruction approaches that utilize different sets of ground truth camera parameters. UnCaliPose [56] uses known camera intrinsics while estimating extrinsics, whereas HAMSt3R [38] and HSfM [29] jointly estimate both intrinsics and extrinsics, with HSfM representing the current state-of-the-art calibration-free method on EgoHumans. We also compare to methods evaluated with both known intrinsics and extrinsics on Human3.6M, including AdaFuse [62] and Iskakov et al. [17], as well as Hewitt et al. [14], which, although

presented as calibration-free, relies on both parameters in this benchmark. Our evaluation considers multiple configurations in which camera parameters are either estimated, provided as ground truth. We also assess performance both with and without modeling lens distortions to quantify their impact on reconstruction accuracy. Tables 1 and 2 report the human reconstruction and camera metrics, respectively. We evaluate HSfM accuracy on Human3.6M using the official code released on the authors’ repository, ensuring evaluation conditions consistent with those used for EgoHumans and EgoExo4D. For full transparency, inference scripts are available at <https://github.com/cjaverliat/hsfm>, and the evaluation code is included in Kineo’s repository.

	Method	Human Metrics		Parameters		
		W-MPJPE↓	PA-MPJPE↓	[R t]	K	d
EgoHumans [19]	UnCaliPose [56]	3.51	0.13	Est.	GT	GT
	HSfM [29]	<u>1.04</u>	<u>0.05</u>	Est.	Est.	-
	HAMSt3R [38]	3.80	0.14	Est.	Est.	-
	Kineo	0.16	0.02	Est.	GT	GT
	Kineo	0.41	0.03	Est.	Est.	-
	Kineo	0.17	0.02	Est.	Est.	Est.
H3.6M [16]	Iskakov et al.	0.02	-	GT	GT	GT
	AdaFuse	0.02	-	GT	GT	GT
	Hewitt et al.	0.03	-	GT	GT	-
	HSfM	<u>0.47</u>	<u>0.05</u>	Est.	Est.	-
	Kineo	0.02	0.02	Est.	GT	GT
	Kineo	0.04	0.02	Est.	Est.	-
Kineo	0.04	0.02	Est.	Est.	Est.	

Table 1. Quantitative comparison of human pose estimation on EgoHumans and Human3.6M. Metrics include mean-per-joint position error in metric world space (W-MPJPE, in meters) and its Procrustes-Aligned version (PA-MPJPE, in meters). For each method, we indicate whether camera parameters are estimated, taken from ground truth, or omitted, where [R|t] denotes the extrinsic camera parameters, K the intrinsic camera matrix (focal length and principal point), and d the distortion coefficients. For each dataset, we highlight the **best** and **second-best calibration-free** methods. **Note:** For HSfM on Human3.6M, results were obtained through our own evaluation, while other values are reported as in the respective papers.

Kineo achieves substantial improvements in both camera estimation and 3D human reconstruction across datasets. On EgoHumans, it surpasses the strongest prior calibration-free baseline, HSfM [29]. In the fully calibration-free setting, where extrinsics, intrinsics, and distortion parameters are all estimated, Kineo achieves a camera translation error of 0.34 m (compared to 2.09 m for HSfM and 2.33 m for HAMSt3R) and an angular error of 0.69° (compared to 9.35° for HSfM and 10.24° for HAMSt3R), while achieving a vertical field-of-view error of 1.03°. These improvements in camera estimation directly enhance human reconstruction quality, attaining a W-MPJPE of 0.17 m (compared to 1.04 m for HSfM and 3.80 m for HAMSt3R) and a PA-MPJPE of 2 cm (compared to 5 cm for HSfM and 14 cm for HAMSt3R). A similar trend is observed on Human3.6M, where Kineo again delivers consistent gains over previous methods. Under the same calibration-free conditions, Kineo achieves a camera translation error of 0.12 m (compared to 0.83 m for HSfM) and an angular error of 0.89° (compared to 6.44° for HSfM). The field-of-view error

Method	Camera Metrics											Parameters		
	TE↓	s-TE↓	AE↓	RRA@10↑	RRA@15↑	CCA@10↑	CCA@15↑	s-CCA@10↑	s-CCA@15↑	FoV↓	[R t]	K	d	
EgoHumans [19]	UnCaliPose [56]	2.63	2.63	60.90	0.28	0.39	-	-	0.33	0.44	-	Est.	GT	GT
	DUST3R [55]	-	1.15	11.00	0.61	0.74	-	-	0.49	0.74	-	Est.	Est.	-
	MASt3R [25]	4.97	0.92	10.42	0.61	0.74	0.06	0.07	0.65	0.86	-	Est.	Est.	-
	HSfM [29]	<u>2.09</u>	<u>0.75</u>	<u>9.35</u>	<u>0.72</u>	<u>0.89</u>	<u>0.32</u>	<u>0.46</u>	<u>0.75</u>	<u>0.91</u>	-	Est.	Est.	-
	HAMSt3R [38]	2.33	0.40	10.24	0.77	-	0.06	-	0.75	-	-	Est.	Est.	-
	Kineo	0.29	0.05	0.34	1.00	1.00	0.99	1.00	0.99	1.00	0.00	Est.	GT	GT
	Kineo	0.76	0.57	3.48	0.91	0.98	0.72	0.90	0.89	0.98	2.96	Est.	Est.	-
Kineo	0.34	0.15	0.69	1.00	1.00	0.98	0.99	0.99	1.00	1.03	Est.	Est.	Est.	
H3.6M [16]	HSfM	0.83	0.33	6.44	0.95	0.96	0.46	0.74	0.95	0.95	36.97	Est.	Est.	-
	Kineo	0.01	0.01	0.20	1.00	1.00	1.00	1.00	1.00	1.00	0.00	Est.	GT	GT
	Kineo	0.13	0.03	0.90	1.00	1.00	1.00	1.00	1.00	1.00	0.57	Est.	Est.	-
	Kineo	0.12	0.02	0.89	1.00	1.00	1.00	1.00	1.00	1.00	0.43	Est.	Est.	Est.

Table 2. Quantitative comparison of camera pose estimation on EgoHumans and Human3.6M. Metrics include translation error (TE, in meters), scale-aligned translation error (s-TE, in meters), angular error (AE, in degrees), Camera Center Accuracy (CCA, as a proportion), scale-aligned CCA (s-CCA, as a proportion), and Relative Rotation Accuracy (RRA, as a proportion). For each dataset we report **first** and **second** calibration-free methods. **Note:** For HSfM on Human3.6M, results were obtained through our own evaluation, while other values are reported as in the respective papers.

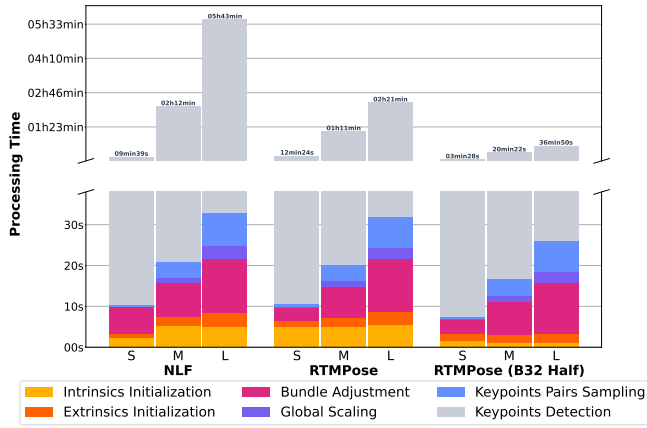


Fig. 9. Automatic calibration runtimes for different keypoint detectors across sequences of varying durations. The comparison includes three keypoint sources: NLF (batch size 1, full precision), RTMPose (batch size 1, full precision), and RTMPose (batch size 32, half precision). Sequence sizes are small (S, 7min10s total across 4 views), medium (M, 43min03s total across 4 views), and long (L, 1h23min total across 4 views). Each stacked bar breaks down the runtime by processing stage: Intrinsic Initialization (yellow), Extrinsic Initialization (orange), Bundle Adjustment (pink), Global Scaling (purple), Keypoints Pairs Sampling (blue), and Keypoints Detection (gray). Total runtime is indicated above each bar. RTMPose (B32 Half) consistently achieves the fastest processing times, completing all stages in less time than the total duration of the original video sequences. Importantly, the calibration runtime scales efficiently, showing only moderate increases as sequence duration grows.

is similarly reduced to 0.43° (compared to 36.97° for HSfM). These improvements in camera estimation directly translate to enhanced human reconstruction quality, yielding a W-MPJPE of 0.04 m (compared to 0.47 m for HSfM) and a PA-MPJPE of 2 cm (compared to 5 cm for HSfM).

To better understand the impact of estimating each camera parameter, we also examined intermediate configurations of Kineo.

Providing ground-truth intrinsics, which can often be obtained from manufacturer specifications or post-capture, consistently improves both camera and human metrics, as expected. On Human3.6M, for instance, access to known intrinsics reduces translation and angular errors from 0.12 m and 0.89° to 0.01 m and 0.20° , and halves the W-MPJPE from 0.04 m to 0.02 m. This performance is competitive with that of fully calibrated methods such as AdaFuse [62] and Isakov et al. [17], indicating that Kineo attains state-of-the-art accuracy with calibrated method, even in the absence of camera extrinsics. Most notably, modeling lens distortion proves critical, especially for EgoHumans, where the wide-angle GoPro cameras introduce significant distortions. When distortion parameters are estimated, Kineo’s camera translation error decreases from 0.76 m to 0.34 m and angular error from 3.48° to 0.69° , with corresponding improvements in reconstruction accuracy, W-MPJPE from 0.41 m to 0.17 m and PA-MPJPE from 0.03 m to 0.02 m. These results highlight that modeling distortions is essential for achieving high-fidelity calibration-free human reconstruction in challenging real-world capture conditions, while also providing the practical benefit of enabling accurate image undistortion for downstream tasks (see Sec. 6.1).

In addition to its accuracy gains, Kineo is computationally efficient and scalable. Figure 9 reports runtimes for different pipeline stages across sequences of varying lengths and four views using multiple keypoint detectors. We evaluated three sequences of increasing length: a small sequence (S) typical of standard datasets, approximately 1 minute in duration; a medium sequence (M) of roughly 10 minutes; and a long sequence (L) of approximately 20 minutes. Three keypoint detection configurations were tested: NLF [39], RTMPose [18] with a batch size of 1 and full precision, and RTMPose with a batch size of 32 and half precision. All experiments using SMPL-based global scaling enabled and were conducted on a single NVIDIA A100 GPU. Across all configurations, keypoint detection is the most time-consuming stage, while the remaining calibration stages scale moderately with sequence length. These results indicate that Kineo’s calibration pipeline is both efficient and scalable, making it suitable for long-duration, real-world captures. For example, when processing a 20-minute, four-view recording using

the RTMPose model for keypoint detection (half precision, batch size = 32), the total processing time is only 36 minutes, substantially shorter than the cumulative duration of the input footage ($4 \times 20 \text{ min} = 1 \text{ h } 20 \text{ min}$).

8.3 Ablation Study

8.3.1 Impact of Camera Parameter Estimation. We conduct an ablation study to assess the impact of estimating different subsets of camera parameters on human and camera metrics. The results are presented in Table 3. Ground-truth 2D human keypoints and global scale are used to eliminate the influence of the 2D detector and the global scale estimation strategy, which are evaluated separately in Sec. 8.3.2 and Sec. 8.3.3.

	Human Metrics		Camera Metrics				Parameters		
	W-MPJPE↓	PA-MPJPE↓	TE↓	s-TE↓	AE↓	FoV↓	[R t]	K	d
EgoHumans [19]	0.006	0.002	0.000	0.000	0.000	0.000	GT	GT	GT
	0.011	0.003	0.010	0.010	0.092	0.000	Est.	GT	GT
	0.311	0.024	0.658	0.658	3.813	2.776	Est.	Est.	-
	0.098	0.007	0.196	0.196	0.993	1.531	Est.	Est.	Est.
Human3.6M [16]	0.000	0.000	0.000	0.000	0.000	0.000	GT	GT	GT
	0.000	0.000	0.000	0.000	0.002	0.000	Est.	GT	GT
	0.014	0.002	0.020	0.020	0.894	0.380	Est.	Est.	-
	0.006	0.001	0.011	0.011	0.863	0.243	Est.	Est.	Est.

Table 3. Ablation study for different combinations of ground truth (GT), estimated (est) parameters and omitted parameters, evaluated on Human3.6M and EgoHumans datasets. We isolate the effect of camera parameters estimation by using ground truth keypoints to simulate an ideal detector and ground-truth global scale.

When all camera parameters are fixed to their ground-truth values, the reported metrics reflect only the residual errors arising from the triangulation process. In this configuration, the pipeline achieves minimal errors in both human and camera metrics, with PA-MPJPE and W-MPJPE approaching zero. It is important to note that our method relies on a simple DLT triangulation, which is not optimal due to its linear approximations; while these residual errors could potentially be reduced further by applying an additional optimization step on the keypoint reprojection error, we did not perform this step for efficiency, as we considered the residual error to be already sufficiently low.

When the intrinsics and distortion coefficients are ground-truth and only the extrinsics parameters are estimated, the resulting metrics reflect the residual errors introduced by the structure-from-motion (SfM) initialization and the first bundle adjustment stage, which optimizes the camera poses. Expanding the estimation to include both extrinsic and intrinsic parameters, while fixing the distortion coefficients to zero (effectively omitting distortion modeling), reveals additional residual errors. These errors arise from the intrinsic parameter initialization and the second bundle adjustment stage, which optimizes the focal length. However, the most significant source of residual error in this configuration is the absence of distortion modeling. This becomes evident when distortions are introduced as an additional parameter to be estimated in the next configuration, leading to a substantial reduction in the overall reconstruction error. For instance, the world mean per joint position error (W-MPJPE) decreases by approximately $\approx 68\%$ on the EgoHumans dataset and $\approx 57\%$ on the Human3.6M dataset.

8.3.2 Impact of 2D Keypoint Detector. Since our method depends on 2D keypoint detections, we assess how the choice of detector affects human reconstruction accuracy through the PA-MPJPE. In this study, all camera parameters are estimated, creating a scenario in which no prior information is provided and the only variable is the selected 2D keypoint detector. The results of this evaluation are reported in Table 4.

	Keypoints	PA-MPJPE↓
EgoHumans [19]	Ground-truth	0.007
	NLF [39]	0.019
	DWPose [59]	0.024
Human3.6M [16]	Ground-truth	0.002
	NLF [39]	0.019
	RTMPose [18]	0.022

Table 4. Impact of 2D detector on the PA-MPJPE (lower is better). All camera parameters are estimated (extrinsics, intrinsics, distortion coefficients).

The choice of detector significantly influences reconstruction performance. As expected, ground-truth keypoints yield the lowest error across all metrics, establishing a performance upper bound. Notably, the PA-MPJPE error drops to 2 mm on Human3.6M and 7 mm on EgoHumans when ground-truth keypoints are used.

When comparing detectors, NLF [39] consistently outperforms DWPose [59] on the EgoHumans dataset and RTMPose [18] on Human3.6M. This demonstrates that, while NLF incurs a higher computational cost, it yields lower errors in human pose estimation. This flexibility in the choice of the keypoints detector allows Kineo to balance the trade-off between accuracy and efficiency based on the specific use case: whether prioritizing maximal accuracy with a more resource-intensive model or opting for a lightweight, faster detector to achieve real-time inference of 2D keypoints.

These results highlight a key advantage of our modular approach: as 2D keypoint detection technology evolves, Kineo can seamlessly integrate advancements without requiring retraining. In contrast, end-to-end models would demand a complete retraining pipeline to incorporate new architectures or improvements. Thus, Kineo is well-positioned to leverage future advancements in 2D keypoint detection.

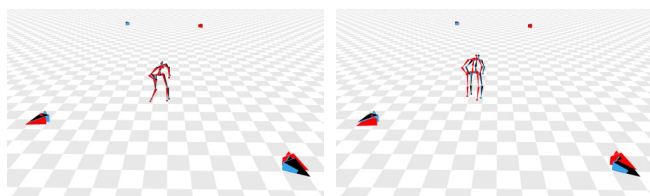
8.3.3 Impact of Global Scaling Strategy. Table 5 presents the ablation study evaluating the impact of the global scale estimation strategy used on reconstruction accuracy and camera metrics. In this analysis, all camera parameters and 2D keypoints are fixed to their ground-truth values, only the global scale factor is computed and applied. This design isolates the effect of scale estimation on the reconstructed scene, independent of errors from camera calibration or 2D keypoint detection.

8.4 Qualitative Evaluation

Figure 10 presents qualitative comparisons between the best sequences obtained with HSfM and Kineo. For each method, we show the sequence with the minimum mean W-MPJPE. In both cases,

	Scaling Method	W-MPJPE ↓	TE ↓
EgoHumans [19]	SMPL-based	0.138	0.252
	Metric Depth-based	0.595	1.074
Human3.6M [16]	SMPL-based	0.021	0.103
	Metric Depth-based	0.145	0.721

Table 5. Ablation study on the impact of different global scale estimation strategies (SMPL-based and metric depth-based using MoGe [54]) on reconstruction accuracy (W-MPJPE) and camera translation error (TE). All camera parameters and 2D keypoints are fixed to ground-truth values, isolating the effect of scale estimation. Results are reported for EgoHumans and Human3.6M datasets.



(a) Frame with the minimum W-MPJPE (0.076 m) from HSfM’s best sequence, *S11_Eating 1*. The overall sequence has a mean W-MPJPE of 0.165 ± 0.276 m. (b) Frame with the minimum W-MPJPE (0.011 m) from Kineo’s best sequence, *S11_WalkTogether 1*. The overall sequence has a mean W-MPJPE of 0.016 ± 0.003 m.

Fig. 10. Qualitative comparison between HSfM (red) and Kineo (blue) on their respective best-performing sequences from Human3.6M. Ground truth camera and skeletons are shown in black. Visualization is scale-aligned.

Kineo shows better camera pose estimation, with lower mean W-MPJPE and standard deviation. The full comparison on all of Human3.6M sequences is available in the supplementary materials.

Figure 11 illustrates qualitative results obtained using Kineo on representative sequences from the EgoHumans dataset, including activities such as badminton, basketball, fencing, lego assembly, tagging, tennis, and volleyball. For each sequence, the scene pointmaps were reconstructed from a single camera view. The images were first undistorted using the estimated distortion coefficients, and the estimated focal length was subsequently provided to MoGe [54] to enhance the accuracy of the reconstruction. Qualitatively, Kineo produces estimated results (in blue) that closely align with the ground truth (in black).

A qualitative example of lens undistortion on EgoHumans is shown in Figure 12. The original GoPro frames exhibit pronounced barrel distortion, particularly visible along the image borders. By estimating and correcting for these distortion, we recover images in which the effects of lens nonlinearity are removed, effectively converting our camera into a pinhole camera model suitable for downstream tasks. This undistortion not only improves the accuracy of multi-view triangulation but also enhances subsequent reconstruction processes, such as scene point cloud generation, all achieved without relying on any ground-truth calibration. Additional qualitative results are provided in the supplementary materials.



(a) Original Distorted Image (b) Undistorted Image (Estimated)

Fig. 12. Qualitative comparison on the EgoHumans *basketball* sequence, showing the distorted input image (left) and the undistorted image obtained using Kineo’s estimated distortion coefficients (right). **Black** lines denote ground-truth distorted/undistorted lines, while **red** lines indicate the undistorted lines reconstructed from Kineo’s estimates, which closely align with the ground truth.

9 Practical Applications

Kineo provides two processing modes: offline and online. The offline mode is the primary mode, designed for unconstrained, real-world video capture, delivering high reconstruction accuracy and supporting long sequences without on-site calibration. The online mode enables real-time processing of live video streams, offering immediate feedback for interactive applications.

9.1 In-The-Wild Capture (Offline Mode)

Kineo enables rapid deployment using battery-powered cameras and eliminates the need for on-site calibration and thereby facilitates outdoor data capture by non-experts within minutes. Kineo was used in a real-world use case to capture the gestures of craftsmen in an experimental archaeology worksite, where a castle is currently being built using medieval techniques. The goal was to preserve this intangible cultural heritage. For this case, the emphasis was placed on reconstruction accuracy, achieved through the use of high-capacity keypoint detection models and spatio-temporal sampling across the entire video sequence.

A notable advantage of Kineo compared to prior works is its capacity to process significantly longer video sequences than those typically found in public datasets, with durations ranging from five to thirty minutes. Two illustrative examples of craftsmen motion capture are presented in Figure 13. Other examples are available in the supplementary materials. These sequences were captured using six uncalibrated and unsynchronized GoPro Hero11 Black cameras, with the entire setup installation completed in approximately ten minutes. All subsequent processing was performed on a local workstation equipped with an NVIDIA RTX 3080 Ti. For instance, a representative five-minute sequence (yielding a cumulative 30 minutes of footage) required approximately 11 minutes for keypoint detection using DWPose, followed by 30 seconds for camera calibration with Kineo. The most computationally demanding stage involved segmentation and cross-view re-identification of individuals using a custom implementation of SAM2, which took approximately 2.5 hours to process all views. This step was optimized to prevent out-of-memory errors, as the original SAM2 lacked effective memory-management strategies. Future work may explore more efficient tracking methods to further reduce processing time for this stage.

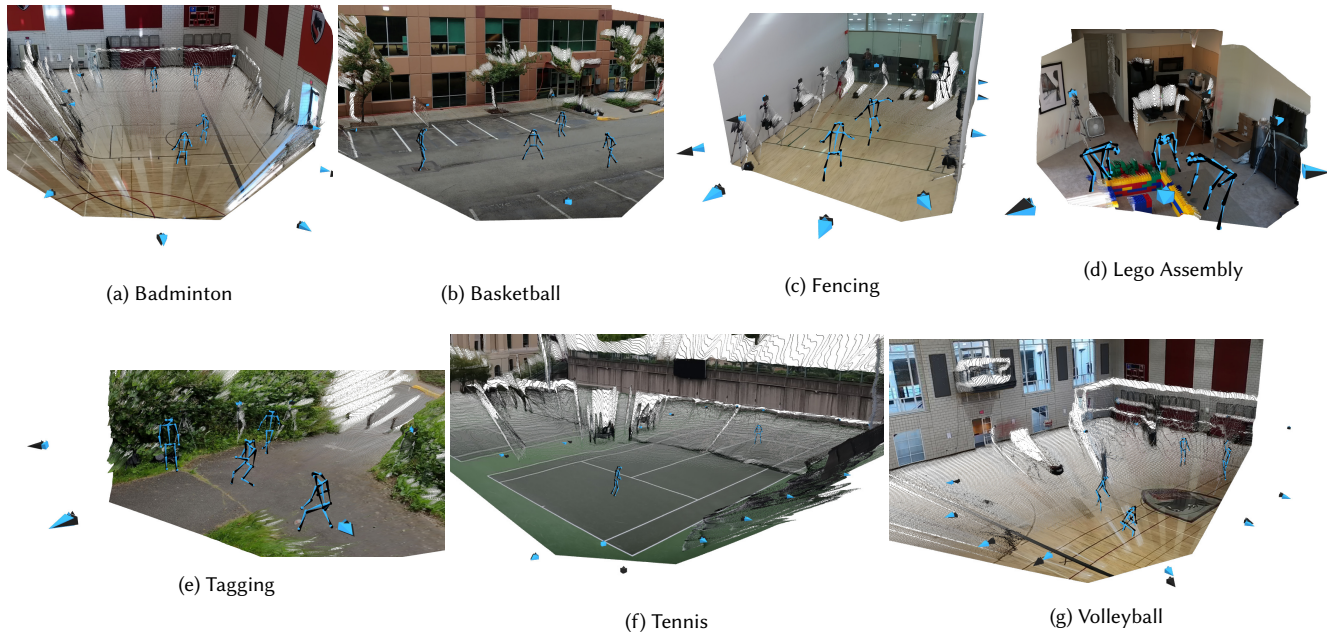


Fig. 11. Qualitative results on sequences from the *EgoHumans* dataset. Kineo estimations are visualized in **blue**, while ground truth cameras and skeletons are shown in **black**. The scene pointmap is predicted as a downstream task of our method using MoGe [54].



Fig. 13. Examples of craftsmen recorded for at an experimental archaeology worksite. Both sequences were captured using six uncalibrated and unsynchronized GoPro Hero11 Black cameras, with no calibration procedure necessary.

9.2 Realtime Capture (Online Mode)

The real-time (online) mode represents an extension of Kineo’s original offline pipeline, specifically designed to process live video streams and provide immediate visual feedback during capture. This mode is particularly advantageous for applications such as interactive motion capture systems and real-time avatar animation.

In this mode, Kineo processes video input directly from multiple webcams. The system first executes the automatic calibration phase, during which a short sequence of approximately 30s to 1min is recorded to estimate camera parameters. Following calibration, Kineo continuously processes incoming frames to detect and reconstruct the subject in real time. Person detection is performed using the RTMDet-tiny model, while 2D keypoint estimation is carried

out with DWPose. These models were selected for their ability to maintain a balance between accuracy and computational efficiency. Videos of live capture are available in the supplementary material.

10 Conclusion

We presented Kineo, a fully automatic, calibration-free pipeline for metric multi-view markerless motion capture that operates on unsynchronized, uncalibrated, consumer RGB cameras. By leveraging a confidence-driven, keypoint-first approach, Kineo identifies the most reliable correspondences across frames and views, enabling robust calibration and reconstruction without the computational cost of per-frame parametric fitting. Its design couples classical SfM geometry with modern keypoint detection, resulting in a modular, scalable, and future-proof system: improvements in 2D detectors directly translate into higher calibration accuracy and 3D fidelity without architectural changes.

Extensive evaluations conducted on the EgoHumans and Human3.6M datasets demonstrate that Kineo significantly reduces the performance gap between calibration-free and calibrated methods, surpassing previous state-of-the-art calibration-free approaches. Moreover, its computational efficiency enables both offline processing of extended video sequences and real-time operation. Notably, Kineo scales effectively to real-world, in-the-wild capture scenarios, achieving processing speeds that, in some configurations, allow it to process videos faster than their actual duration.

Looking forward, we identify several promising research directions. First, integrating the proposed 3D confidence scores into temporal filtering could enhance robustness and temporal coherence. Second, camera pose estimation could be further refined by incorporating a photometric loss, following Choi et al. [6], who

demonstrated that dynamic NeRF optimization can be used to jointly refine camera poses and reconstruct volumetric representations of the scenes.

Acknowledgments

This work was supported by the Auvergne-Rhône-Alpes region as part of the PROMESS project. This work was granted access to the HPC resources of IDRIS under the allocation 2025-AD010614830 made by GENCI. We also express our gratitude to the Guédelon Castle for kindly welcoming us and permitting the captures that were essential to this study.

References

- [1] Ijaz Akhter, Tomas Simon, Sohaib Khan, Iain Matthews, and Yaser Sheikh. 2012. Bilinear Spatiotemporal Basis Models. *ACM Transactions on Graphics* 31, 2 (2012), 17:1–17:12. doi:10.1145/2159516.2159523
- [2] Federica Arrigoni, Andrea Fusiello, and Beatrice Rossi. 2015. On Computing the Translations Norm in the Epipolar Graph. In *2015 International Conference on 3D Vision*. 300–308. doi:10.1109/3DV.2015.41
- [3] Fabien Baradel, Matthieu Armando, Salma Galaoui, Romain Brégier, Philippe Weinzaepfel, Grégory Rogez, and Thomas Lucas. 2025. Multi-HMR: Multi-person Whole-Body Human Mesh Recovery in a Single Shot. In *Computer Vision – ECCV 2024*, Aleš Leonardis, Elisa Ricci, Stefan Roth, Olga Russakovsky, Torsten Sattler, and Gül Varol (Eds.). Springer Nature Switzerland, Cham, 202–218.
- [4] Oleksandr Bogdan, Viktor Eckstein, Francois Rameau, and Jean-Charles Bazin. 2018. DeepCalib: a deep learning approach for automatic intrinsic calibration of wide field-of-view cameras. In *Proceedings of the 15th ACM SIGGRAPH European Conference on Visual Media Production (London, United Kingdom) (CVMP '18)*. Association for Computing Machinery, New York, NY, USA, Article 6, 10 pages. doi:10.1145/3278471.3278479
- [5] Laura Bragagnolo, Matteo Terreran, Davide Allegro, and Stefano Ghidoni. 2025. Multi-view Pose Fusion for Occlusion-Aware 3D Human Pose Estimation. In *Computer Vision – ECCV 2024 Workshops: Milan, Italy, September 29–October 4, 2024, Proceedings, Part XII* (Milan, Italy). Springer-Verlag, Berlin, Heidelberg, 117–133. arXiv:2408.15810 doi:10.1007/978-3-031-92591-7_8
- [6] Changwoon Choi, Jeongjun Kim, Geonho Cha, Minkwan Kim, Dongyoon Wee, and Young Min Kim. 2025. Humans as a Calibration Pattern: Dynamic 3D Scene Reconstruction from Unsynchronized and Uncalibrated Videos. In *Proceedings of the IEEE/CVF International Conference on Computer Vision (ICCV)*.
- [7] Sai Kumar Dwivedi, Cordelia Schmid, Hongwei Yi, Michael J. Black, and Dimitrios Tzionas. 2024. POCO: 3D Pose and Shape Estimation with Confidence. In *2024 International Conference on 3D Vision (3DV)*. IEEE Computer Society, Los Alamitos, CA, USA, 85–95. doi:10.1109/3DV62453.2024.00115
- [8] Sai Kumar Dwivedi, Yu Sun, Priyanka Patel, Yao Feng, and Michael J. Black. 2024. TokenHMR: Advancing Human Mesh Recovery with a Tokenized Pose Representation. In *2024 IEEE/CVF Conference on Computer Vision and Pattern Recognition (CVPR)*. 1323–1333. doi:10.1109/CVPR52733.2024.00132
- [9] Shubham Goel, Georgios Pavlakos, Jathushan Rajasegaran, Angjoo Kanazawa, and Jitendra Malik. 2023. Humans in 4D: Reconstructing and Tracking Humans with Transformers. In *2023 IEEE/CVF International Conference on Computer Vision (ICCV)*. IEEE Computer Society, Los Alamitos, CA, USA, 14737–14748. doi:10.1109/ICCV51070.2023.01358
- [10] Richard I. Hartley. 1997. Kruppa's Equations Derived from the Fundamental Matrix. *IEEE Trans. Pattern Anal. Mach. Intell.* 19, 2 (Feb. 1997), 133–135. doi:10.1109/34.574792
- [11] Nils Hasler, Bodo Rosenhahn, Thorsten Thormahlen, Michael Wand, Juergen Gall, and Hans-Peter Seidel. 2009. Markerless Motion Capture with Unsynchronized Moving Cameras. In *2009 IEEE Conference on Computer Vision and Pattern Recognition (Miami, FL, 2009-06)*. IEEE, 224–231. doi:10.1109/CVPR.2009.5206859
- [12] Charlie Hewitt, Tadas Baltrušaitis, Erroll Wood, Lohit Petikam, Louis Florentin, and Hanz Cuevas Velasquez. 2024. Procedural Humans for Computer Vision. arXiv:2301.01161 [cs.CV] <https://arxiv.org/abs/2301.01161>
- [13] Charlie Hewitt, Fatemeh Saleh, Sadeh Aliakbarian, Lohit Petikam, Shideh Rezaei-far, Louis Florentin, Zafira Hosenie, Thomas J. Cashman, Julien Valentin, Darren Cosker, and Tadas Baltrušaitis. 2024. Look Ma, no markers: holistic performance capture without the hassle. *ACM Transactions on Graphics* 43, 6, Article 235 (Nov. 2024), 12 pages. doi:10.1145/3687772
- [14] Charlie Hewitt, Fatemeh Saleh, Sadeh Aliakbarian, Lohit Petikam, Shideh Rezaei-far, Louis Florentin, Zafira Hosenie, Thomas J. Cashman, Julien Valentin, Darren Cosker, and Tadas Baltrušaitis. 2024. Look Ma, No Markers: Holistic Performance Capture without the Hassle. *ACM Transactions on Graphics* 43, 6 (2024), 1–12. doi:10.1145/3687772
- [15] Yinghao Huang, Federica Bogo, Christoph Lassner, Angjoo Kanazawa, Peter V. Gehler, Javier Romero, Ijaz Akhter, and Michael J. Black. 2017. Towards Accurate Marker-Less Human Shape and Pose Estimation over Time. In *2017 International Conference on 3D Vision (3DV)*. 421–430. arXiv:1707.07548 doi:10.1109/3DV.2017.00055
- [16] Catalin Ionescu, Dragos Papava, Vlad Olaru, and Cristian Sminchisescu. 2014. Human3.6M: Large Scale Datasets and Predictive Methods for 3D Human Sensing in Natural Environments. *IEEE Transactions on Pattern Analysis and Machine Intelligence* 36, 7 (2014), 1325–1339. doi:10.1109/TPAMI.2013.248
- [17] Karim Iskakov, Egor Burkov, Victor Lempitsky, and Yury Malkov. 2019. Learnable Triangulation of Human Pose. In *2019 IEEE/CVF International Conference on Computer Vision (ICCV)*. 7717–7726. doi:10.1109/ICCV.2019.00781
- [18] Tao Jiang, Peng Lu, Li Zhang, Ningsheng Ma, Rui Han, Chengqi Lyu, Yining Li, and Kai Chen. 2023. RTMPose: Real-Time Multi-Person Pose Estimation based on MMPose. doi:10.48550/ARXIV.2303.07399
- [19] Rawal Khrodgar, Aayush Bansal, Lingni Ma, Richard Newcombe, Minh Vo, and Kris Kitani. 2023. EgoHumans: An Egocentric 3D Multi-Human Benchmark. In *2023 IEEE/CVF International Conference on Computer Vision (ICCV)*. 19750–19762. doi:10.1109/ICCV51070.2023.01814
- [20] Muhammed Kocabas, Chun-Hao P Huang, Joachim Tesch, Lea Müller, Otmar Hilliges, and Michael J. Black. 2021. SPEC: Seeing People in the Wild with an Estimated Camera. In *2021 IEEE/CVF International Conference on Computer Vision (ICCV)*. 11015–11025. arXiv:2110.00620 doi:10.1109/ICCV48922.2021.01085
- [21] Nikos Kolotouros, Georgios Pavlakos, Dinesh Jayaraman, and Kostas Daniilidis. 2021. Probabilistic Modeling for Human Mesh Recovery. In *2021 IEEE/CVF International Conference on Computer Vision (ICCV)*. IEEE Computer Society, Los Alamitos, CA, USA, 11585–11594. doi:10.1109/ICCV48922.2021.01140
- [22] N. Krahnstoever and P.R.S. Mendonca. 2005. Bayesian Autocalibration for Surveillance. In *Tenth IEEE International Conference on Computer Vision (ICCV'05) Volume 1 (2005-10)*, Vol. 2. 1858–1865 Vol. 2. doi:10.1109/ICCV.2005.44
- [23] Erwin Kruppa. 1913. To determine a 3D object from two perspective views with known inner orientation. *Proceedings of the Imperial Academy of Sciences, Mathematics and Natural Sciences* 122 (1913), 1939–1948.
- [24] Richard Latimer, Jason Holloway, Ashok Veeraraghavan, and Ashutosh Sabharwal. 2015. SocialSync: Sub-Frame Synchronization in a Smartphone Camera Network. In *Computer Vision – ECCV 2014 Workshops*, Lourdes Agapito, Michael M. Bronstein, and Carsten Rother (Eds.). Springer International Publishing, Cham, 561–575. doi:10.1007/978-3-319-16181-5_43
- [25] Vincent Leroy, Johann Cabon, and Jerome Revaud. 2024. Grounding Image Matching in 3D with MAST3R. In *Lecture Notes in Computer Science (Milan, Italy)*. Springer Nature Switzerland, Berlin, Heidelberg, 71–91. doi:10.1007/978-3-031-73220-1_5
- [26] Amy Lin, Jason Y. Zhang, Deva Ramanan, and Shubham Tulsiani. 2024. RelPose++: Recovering 6D Poses from Sparse-view Observations. In *2024 International Conference on 3D Vision (3DV)*. 106–115. doi:10.1109/3DV62453.2024.00126
- [27] Matthew Loper, Naureen Mahmood, Javier Romero, Gerard Pons-Moll, and Michael J. Black. 2015. SMPL: a skinned multi-person linear model. *ACM Trans. Graph.* 34, 6, Article 248 (Nov. 2015), 16 pages. doi:10.1145/2816795.2818013
- [28] Fengjun Lv, Tao Zhao, and R. Nevatia. 2006. Camera Calibration from Video of a Walking Human. *IEEE Transactions on Pattern Analysis and Machine Intelligence* 28, 9 (2006), 1513–1518. doi:10.1109/TPAMI.2006.178
- [29] Lea Müller, Hongsuk Choi, Anthony Zhang, Brent Yi, Jitendra Malik, and Angjoo Kanazawa. 2025. Reconstructing People, Places, and Cameras. In *Proceedings of the Computer Vision and Pattern Recognition Conference (CVPR)*. 21948–21958. arXiv:2412.17806 <https://arxiv.org/abs/2412.17806>
- [30] NaturalPoint. 2025. Optitrack Motion Capture Systems. <https://www.optitrack.com>. Accessed: July 23, 2025.
- [31] D. Nister. 2004. An efficient solution to the five-point relative pose problem. *IEEE Transactions on Pattern Analysis and Machine Intelligence* 26, 6 (2004), 756–770. doi:10.1109/TPAMI.2004.17
- [32] Priyanka Patel and Michael J. Black. 2025. CameraHMR: Aligning People with Perspective. In *2025 International Conference on 3D Vision (3DV)*. IEEE Computer Society, Los Alamitos, CA, USA, 1562–1571. doi:10.1109/3DV66043.2025.00146
- [33] Georgios Pavlakos, Vasileios Choutas, Nima Ghorbani, Timo Bolkart, Ahmed A. Osman, Dimitrios Tzionas, and Michael J. Black. 2019. Expressive Body Capture: 3D Hands, Face, and Body From a Single Image. In *2019 IEEE/CVF Conference on Computer Vision and Pattern Recognition (CVPR)*. IEEE Computer Society, Los Alamitos, CA, USA, 10967–10977. doi:10.1109/CVPR.2019.01123
- [34] Jens Puwein, Luca Ballan, Remo Ziegler, and Marc Pollefeys. 2015. Joint Camera Pose Estimation and 3D Human Pose Estimation in a Multi-camera Setup. In *Computer Vision – ACCV 2014*, Daniel Cremers, Ian Reid, Hideo Saito, and Ming-Hsuan Yang (Eds.). Vol. 9004. Springer International Publishing, 473–487. doi:10.1007/978-3-319-16808-1_32
- [35] Haibo Qiu, Chunyu Wang, Jingdong Wang, Naiyan Wang, and Wenjun Zeng. 2019. Cross View Fusion for 3D Human Pose Estimation. In *2019 IEEE/CVF International*

- Conference on Computer Vision (ICCV)*. 4341–4350. doi:10.1109/ICCV.2019.00444
- [36] Qualisys. 2025. Qualisys Motion Capture Systems. <https://www.qualisys.com>. Accessed: July 23, 2025.
- [37] Nikhila Ravi, Valentin Gabeur, Yuan-Ting Hu, Ronghang Hu, Chaitanya Ryali, Tengyu Ma, Haitham Khedr, Roman Rädle, Chloe Rolland, Laura Gustafson, Eric Mintun, Junting Pan, Kalyan Vasudev Alwala, Nicolas Carion, Chao-Yuan Wu, Ross Girshick, Piotr Dollár, and Christoph Feichtenhofer. 2024. SAM 2: Segment Anything in Images and Videos. arXiv:2408.00714 [cs.CV] <https://arxiv.org/abs/2408.00714>
- [38] Sara Rojas, Matthieu Armando, Bernard Ghamen, Philippe Weinzaepfel, Vincent Leroy, and Gregory Rogez. 2025. HAMSt3R: Human-Aware Multi-view Stereo 3D Reconstruction. In *Proceedings of the IEEE/CVF International Conference on Computer Vision (ICCV)*. arXiv:2508.16433 <https://arxiv.org/abs/2508.16433>
- [39] István Sárádi and Gerard Pons-Moll. 2025. Neural localizer fields for continuous 3D human pose and shape estimation. In *Proceedings of the 38th International Conference on Neural Information Processing Systems (Vancouver, BC, Canada) (NIPS '24)*. Curran Associates Inc., Red Hook, NY, USA, Article 4444, 34 pages. arXiv:2407.07532
- [40] Johannes Lutz Schönberger and Jan-Michael Frahm. 2016. Structure-from-Motion Revisited. In *Conference on Computer Vision and Pattern Recognition (CVPR)*.
- [41] Akash Sengupta, Ignas Budvytis, and Roberto Cipolla. 2020. Synthetic Training for Accurate 3D Human Pose and Shape Estimation in the Wild. In *British Machine Vision Conference (BMVC)*. arXiv:2009.10013 doi:10.48550/arXiv.2009.10013
- [42] Akash Sengupta, Ignas Budvytis, and Roberto Cipolla. 2023. HuManiFlow: Ancestor-Conditioned Normalising Flows on SO(3) Manifolds for Human Pose and Shape Distribution Estimation. In *2023 IEEE/CVF Conference on Computer Vision and Pattern Recognition (CVPR)*. IEEE Computer Society, Los Alamitos, CA, USA, 4779–4789. doi:10.1109/CVPR52729.2023.00463
- [43] Prarthana Shrestha, Mauro Barbieri, and Hans Weda. 2007. Synchronization of Multi-Camera Video Recordings Based on Audio. In *Proceedings of the 15th ACM International Conference on Multimedia (New York, NY, USA, 2007-09-29) (MM '07)*. Association for Computing Machinery, 545–548. doi:10.1145/1291233.1291367
- [44] Qing Shuai, Chen Geng, Qi Fang, Sida Peng, Wenhao Shen, Xiaowei Zhou, and Hujun Bao. 2022. Novel View Synthesis of Human Interactions from Sparse Multi-view Videos. In *Special Interest Group on Computer Graphics and Interactive Techniques Conference Proceedings (Vancouver BC Canada, 2022-08-07)*. ACM, 1–10. doi:10.1145/3528233.3530704
- [45] Stanislaw Szymanowicz, Virginia Estellers, Tadas Baltrušaitis, and Matthew Johnson. 2022. Photo-Realistic 360° Head Avatars in the Wild. In *Computer Vision – ECCV 2022 Workshops: Tel Aviv, Israel, October 23–27, 2022, Proceedings, Part III (Tel Aviv, Israel)*. Springer-Verlag, Berlin, Heidelberg, 660–667. doi:10.1007/978-3-031-25066-8_38
- [46] Tentacle Sync. 2025. Tentacle Sync. <https://tentaclesync.com>. Accessed: July 23, 2025.
- [47] Javier Tirado-Garín and Javier Civera. 2025. AnyCalib: On-Manifold Learning for Model-Agnostic Single-View Camera Calibration. In *ICCV*.
- [48] Tsuhan Chen, Alberto Del Bimbo, Federico Pernici, and Giuseppe Serra. 2007. Accurate Self-Calibration of Two Cameras by Observations of a Moving Person on a Ground Plane. In *2007 IEEE Conference on Advanced Video and Signal Based Surveillance (London, UK)*. IEEE, 129–134. doi:10.1109/AVSS.2007.4425298
- [49] Hanyue Tu, Chunyu Wang, and Wenjun Zeng. 2020. VoxelPose: Towards Multi-camera 3D Human Pose Estimation in Wild Environment. In *Computer Vision – ECCV 2020: 16th European Conference, Glasgow, UK, August 23–28, 2020, Proceedings, Part I (Glasgow, United Kingdom)*. Springer-Verlag, Berlin, Heidelberg, 197–212. doi:10.1007/978-3-030-58452-8_12
- [50] Alexander Veicht, Paul-Edouard Sarlin, Philipp Lindenberger, and Marc Pollefeys. 2024. GeoCalib: Learning Single-Image Calibration with Geometric Optimization. In *Computer Vision – ECCV 2024: 18th European Conference, Milan, Italy, September 29–October 4, 2024, Proceedings, Part XL (Milan, Italy)*. Springer-Verlag, Berlin, Heidelberg, 1–20. doi:10.1007/978-3-031-73661-2_1
- [51] Vicon Motion Systems. 2025. Vicon Motion Capture Systems. <https://www.vicon.com>. Accessed: July 23, 2025.
- [52] Minh Vo, Yaser Sheikh, and Srinivasa G. Narasimhan. 2022. Spatiotemporal Bundle Adjustment for Dynamic 3D Human Reconstruction in the Wild. *IEEE Transactions on Pattern Analysis & Machine Intelligence* 44, 2 (Feb. 2022), 1066–1080. doi:10.1109/TPAMI.2020.3012429
- [53] Jianyuan Wang, Minghao Chen, Nikita Karaev, Andrea Vedaldi, Christian Rupprecht, and David Novotny. 2025. VGGT: Visual Geometry Grounded Transformer. In *2025 IEEE/CVF Conference on Computer Vision and Pattern Recognition (CVPR)*. 5294–5306. doi:10.1109/CVPR52734.2025.00499
- [54] Ruicheng Wang, Sicheng Xu, Yue Dong, Yu Deng, Jianfeng Xiang, Zelong Lv, Guangzhong Sun, Xin Tong, and Jiaolong Yang. 2025. MoGe-2: Accurate Monocular Geometry with Metric Scale and Sharp Details. arXiv:2507.02546 [cs.CV] <https://arxiv.org/abs/2507.02546>
- [55] Shuzhe Wang, Vincent Leroy, Yohann Cabon, Boris Chidlovskii, and Jerome Revaud. 2024. DUST3R: Geometric 3D Vision Made Easy. In *2024 IEEE/CVF Conference on Computer Vision and Pattern Recognition (CVPR)*. 20697–20709. doi:10.1109/CVPR52733.2024.01956
- [56] Yan Xu and Kris Kitani. 2022. Multi-View Multi-Person 3D Pose Estimation with Uncalibrated Camera Networks. In *33rd British Machine Vision Conference 2022, BMVC 2022, London, UK, November 21–24, 2022*. BMVA Press. <https://bmvc2022.mpi-inf.mpg.de/0132.pdf>
- [57] Yan Xu, Yu-Jhe Li, Xinshuo Weng, and Kris Kitani. 2021. Wide-Baseline Multi-Camera Calibration using Person Re-Identification. In *2021 IEEE/CVF Conference on Computer Vision and Pattern Recognition (CVPR)*. 13129–13138. arXiv:2104.08568 doi:10.1109/CVPR46437.2021.01293
- [58] Yufei Xu, Jing Zhang, Qiming Zhang, and Dacheng Tao. 2022. ViTPose: Simple Vision Transformer Baselines for Human Pose Estimation. In *Advances in Neural Information Processing Systems*.
- [59] Zhendong Yang, Ailing Zeng, Chun Yuan, and Yu Li. 2023. Effective whole-body pose estimation with two-stages distillation. In *Proceedings of the IEEE/CVF International Conference on Computer Vision*. 4210–4220.
- [60] Hang Ye, Wentao Zhu, Chunyu Wang, Rujie Wu, and Yizhou Wang. 2022. Faster VoxelPose: Real-time 3D Human Pose Estimation by Orthographic Projection. In *Computer Vision – ECCV 2022: 17th European Conference, Tel Aviv, Israel, October 23–27, 2022, Proceedings, Part VI (Tel Aviv, Israel)*. Springer-Verlag, Berlin, Heidelberg, 142–159. doi:10.1007/978-3-031-20068-7_9
- [61] Vickie Ye, Georgios Pavlakos, Jitendra Malik, and Angjoo Kanazawa. 2023. Decoupling Human and Camera Motion from Videos in the Wild. In *2023 IEEE/CVF Conference on Computer Vision and Pattern Recognition (CVPR)*. 21222–21232. doi:10.1109/CVPR52729.2023.02033
- [62] Zhe Zhang, Chunyu Wang, Weichao Qiu, Wenhao Qin, and Wenjun Zeng. 2021. AdaFuse: Adaptive Multiview Fusion for Accurate Human Pose Estimation in the Wild. *Int. J. Comput. Vision* 129, 3 (March 2021), 703–718. doi:10.1007/s11263-020-01398-9

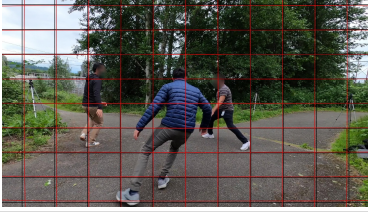
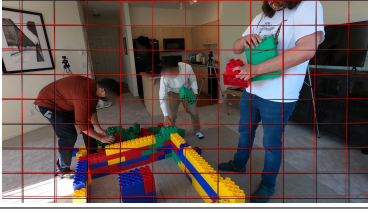
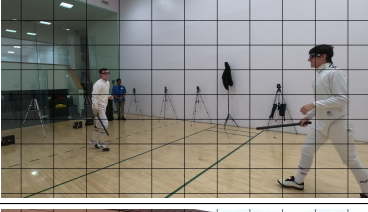
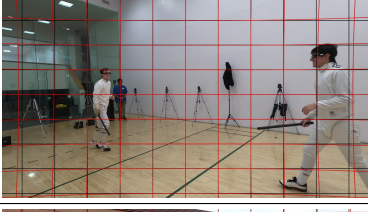
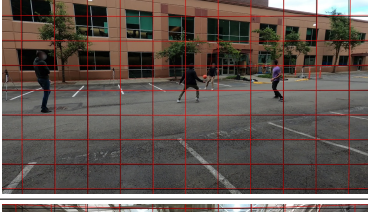
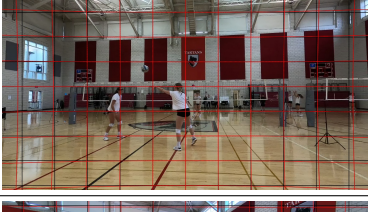
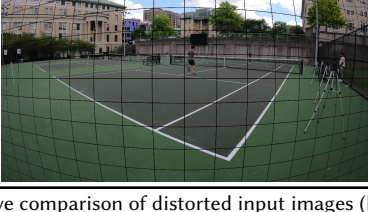
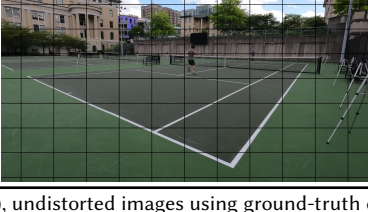
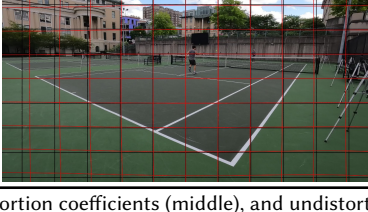
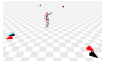
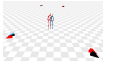
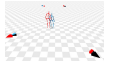
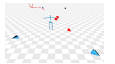
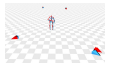
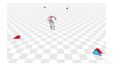
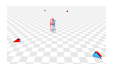
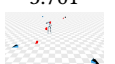
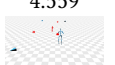
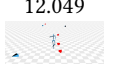
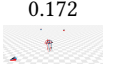
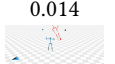
Sequence	Original Image	Undistorted Image (Ground-truth)	Undistorted Image (Estimated)
Tagging			
Lego			
Fencing			
Basketball			
Volleyball			
Badminton			
Tennis			

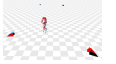
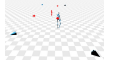
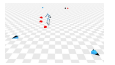
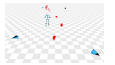
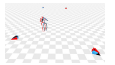
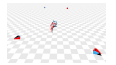
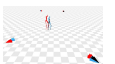
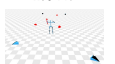
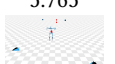
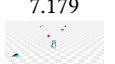
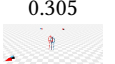
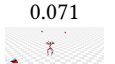
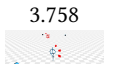
Table 6. Qualitative comparison of distorted input images (left), undistorted images using ground-truth distortion coefficients (middle), and undistorted images using estimated coefficients (right) across multiple sequences from the EgoHumans dataset. Black lines indicate ground-truth distorted/undistorted lines, while red lines show the undistorted lines obtained with distortion parameters estimated by Kineo.

Table 7: Comparison of the W-MPJPE metric (lower is better) across Human3.6M sequences for Kineo (blue), HSfM (red), and ground truth (black). For each sequence, the table reports the minimum, median, maximum, mean, and standard deviation of W-MPJPE over all frames, along with visualizations of the corresponding frames. All estimates are scale-aligned for visualization. Overall, Kineo achieves lower W-MPJPE and demonstrates greater robustness with smaller standard deviation compared to HSfM.

Sequence	HSfM W-MPJPE				Kineo W-MPJPE			
	Min ↓	Median ↓	Max ↓	Mean±Std ↓	Min ↓	Median ↓	Max ↓	Mean±Std ↓
S9_Directions 1	0.144 	0.283 	13.112 	0.693±2.007	0.026 	0.036 	0.066 	0.036±0.006
S11_Directions 1	0.122 	0.167 	11.841 	0.450±1.375	0.046 	0.050 	0.053 	0.050±0.001
S9_Directions	0.138 	0.270 	12.893 	1.679±3.633	0.027 	0.036 	0.058 	0.037±0.005
S11_Directions	0.143 	0.208 	3.127 	0.225±0.207	0.036 	0.040 	0.048 	0.040±0.002
S11_Discussion 2	0.103 	0.172 	12.000 	0.670±1.832	0.021 	0.027 	0.042 	0.028±0.004
S9_Eating 1	0.083 	0.246 	4.316 	0.261±0.247	0.036 	0.045 	0.091 	0.051±0.014
S11_Eating 1	0.076 	0.136 	3.761 	0.165±0.276	0.017 	0.024 	0.037 	0.024±0.003
S9_Eating	0.083 	0.231 	4.559 	0.248±0.262	0.035 	0.044 	0.086 	0.048±0.012
S11_Eating	0.061 	0.137 	9.391 	0.198±0.546	0.018 	0.027 	0.041 	0.027±0.004
S11_Greeting 2	0.080 	0.171 	12.049 	0.857±2.343	0.018 	0.025 	0.039 	0.026±0.004
S11_Greeting	0.083 	0.172 	10.481 	0.462±1.236	0.014 	0.020 	0.047 	0.021±0.004
S9_Phoning 1	0.091 	0.200 	4.507 	0.223±0.342	0.030 	0.043 	0.064 	0.044±0.007

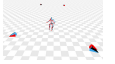
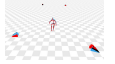
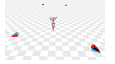
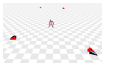
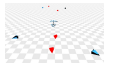
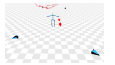
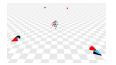
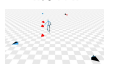
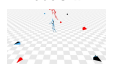
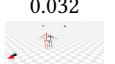
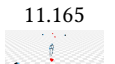
Continued on next page

Table 7: Comparison of the W-MPJPE metric (lower is better) across Human3.6M sequences for Kineo (blue), HSfM (red), and ground truth (black). For each sequence, the table reports the minimum, median, maximum, mean, and standard deviation of W-MPJPE over all frames, along with visualizations of the corresponding frames. All estimates are scale-aligned for visualization. Overall, Kineo achieves lower W-MPJPE and demonstrates greater robustness with smaller standard deviation compared to HSfM. (Continued)

Sequence	HSfM W-MPJPE				Kineo W-MPJPE			
	Min ↓	Median ↓	Max ↓	Mean±Std ↓	Min ↓	Median ↓	Max ↓	Mean±Std ↓
S11_Phoning 3	0.067 	0.163 	7.464 	0.252±0.478	0.014 	0.020 	0.041 	0.021±0.004
S9_Phoning	0.090 	0.192 	4.523 	0.253±0.461	0.029 	0.040 	0.063 	0.042±0.006
S11_Phoning 2	0.047 	0.142 	4.623 	0.188±0.255	0.014 	0.019 	0.029 	0.019±0.003
S9_Posing 1	0.145 	0.282 	12.729 	0.858±2.445	0.029 	0.036 	0.047 	0.036±0.004
S11_Posing 1	0.080 	0.154 	4.729 	0.449±0.874	0.021 	0.027 	0.037 	0.028±0.003
S9_Posing	0.130 	0.291 	11.036 	0.563±1.171	0.031 	0.037 	0.059 	0.039±0.006
S11_Posing	0.106 	0.170 	5.765 	0.684±1.242	0.025 	0.030 	0.039 	0.031±0.003
S9_Purchases 1	0.131 	0.232 	4.635 	0.285±0.318	0.032 	0.038 	0.086 	0.042±0.011
S11_Purchases 1	0.112 	0.182 	7.179 	0.358±0.667	0.019 	0.025 	0.034 	0.025±0.003
S9_Purchases	0.135 	0.305 	12.024 	0.377±0.729	0.034 	0.040 	0.093 	0.046±0.014
S9_Sitting 1	0.119 	0.234 	0.564 	0.245±0.067	0.071 	0.084 	0.102 	0.085±0.005
S11_Sitting 1	0.071 	0.198 	3.758 	0.256±0.256	0.031 	0.037 	0.051 	0.038±0.003

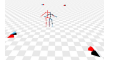
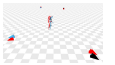
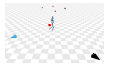
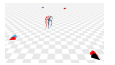
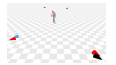
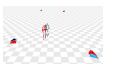
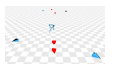
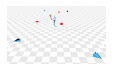
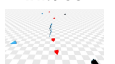
Continued on next page

Table 7: Comparison of the W-MPJPE metric (lower is better) across Human3.6M sequences for Kineo (blue), HSfM (red), and ground truth (black). For each sequence, the table reports the minimum, median, maximum, mean, and standard deviation of W-MPJPE over all frames, along with visualizations of the corresponding frames. All estimates are scale-aligned for visualization. Overall, Kineo achieves lower W-MPJPE and demonstrates greater robustness with smaller standard deviation compared to HSfM. (Continued)

Sequence	HSfM W-MPJPE				Kineo W-MPJPE			
	Min ↓	Median ↓	Max ↓	Mean±Std ↓	Min ↓	Median ↓	Max ↓	Mean±Std ↓
S9_Sitting	0.128 	0.241 	0.496 	0.248±0.064	0.048 	0.057 	0.074 	0.058±0.004
S11_Sitting	0.068 	0.243 	0.626 	0.262±0.134	0.018 	0.025 	0.045 	0.025±0.004
S11_SittingDown 1	0.098 	0.820 	9.471 	0.949±0.942	0.031 	0.041 	0.053 	0.041±0.004
S9_Smoking 1	0.072 	0.189 	12.239 	0.211±0.421	0.028 	0.041 	0.064 	0.042±0.008
S11_Smoking 2	0.068 	0.169 	4.724 	0.262±0.425	0.012 	0.019 	0.034 	0.019±0.003
S9_Smoking	0.071 	0.176 	2.860 	0.180±0.110	0.024 	0.034 	0.059 	0.035±0.006
S9_Photo 1	0.094 	0.248 	11.388 	0.313±0.730	0.027 	0.037 	0.055 	0.039±0.008
S11_Photo 1	0.055 	0.178 	13.303 	0.579±1.532	0.014 	0.023 	0.032 	0.023±0.004
S9_Photo	0.099 	0.253 	13.131 	0.585±1.762	0.032 	0.040 	0.057 	0.041±0.005
S11_Photo	0.069 	0.181 	14.154 	0.751±2.131	0.020 	0.027 	0.036 	0.027±0.003
S11_Waiting 1	0.110 	0.171 	6.420 	0.287±0.637	0.044 	0.048 	0.061 	0.049±0.002
S11_Waiting	0.104 	0.158 	11.165 	0.416±1.457	0.037 	0.041 	0.051 	0.042±0.002

Continued on next page

Table 7: Comparison of the W-MPJPE metric (lower is better) across Human3.6M sequences for Kineo (**blue**), HSfM (**red**), and ground truth (**black**). For each sequence, the table reports the minimum, median, maximum, mean, and standard deviation of W-MPJPE over all frames, along with visualizations of the corresponding frames. All estimates are scale-aligned for visualization. Overall, Kineo achieves lower W-MPJPE and demonstrates greater robustness with smaller standard deviation compared to HSfM. (Continued)

Sequence	HSfM W-MPJPE				Kineo W-MPJPE			
	Min ↓	Median ↓	Max ↓	Mean±Std ↓	Min ↓	Median ↓	Max ↓	Mean±Std ↓
S9_Walking 1	0.065 	0.185 	10.694 	0.249±0.570	0.033 	0.054 	0.087 	0.055±0.012
S9_Walking	0.068 	0.193 	14.010 	0.415±1.505	0.033 	0.053 	0.078 	0.054±0.011
S9_WalkDog 1	0.065 	0.193 	12.397 	0.314±0.947	0.030 	0.047 	0.072 	0.047±0.007
S11_WalkDog 1	0.044 	0.199 	11.408 	1.610±2.684	0.020 	0.027 	0.041 	0.028±0.004
S9_WalkDog	0.059 	0.237 	11.765 	0.390±0.954	0.031 	0.048 	0.070 	0.048±0.008
S9_WalkTogether 1	0.068 	0.203 	4.962 	0.267±0.508	0.033 	0.052 	0.082 	0.053±0.012
S11_WalkTogether 1	0.062 	0.141 	13.837 	0.386±1.263	0.011 	0.015 	0.025 	0.016±0.003
S11_WalkTogether	0.054 	0.136 	12.240 	0.231±0.817	0.012 	0.016 	0.027 	0.017±0.003